Where and How the East Madagascar Current Retroflection Originates?

Juliano D. Ramanantsoa, P. Penven, R. P. Raj, L. Renault, L. Ponsoni, M. Ostrowski, A. F. Dilmahamod, M. Rouault

JGR Oceans

RESEARCH ARTICLE
10.1029/2020JC016203

Where and How the East Madagascar Current Retroflection Originates?

Juliano D. Ramanantsoa[1,2,3,4], P. Penven[5], R. P. Raj[6], L. Renault[7,8], L. Ponsoni[9], M. Ostrowski[10], A. F. Dilmahamod[11,12], and M. Rouault[1,3]

[1]Department of Oceanography, University of Cape Town (UCT), Cape Town, South Africa, [2]Norwegian Research Center (NORCE), Bergen, Norway, [3]Nansen Tutu for Marine Environmental Research, University of Cape Town (UCT), Ma-Re Institute, Cape Town, South Africa, [4]Institut Halieutique et des Sciences Marines (IH.SM), Toliara, Madagascar, [5]Laboratoire d'Océanographie Physique et Spatiale (LOPS), University of Brest, CNRS, IRD, Ifremer, IUEM, Brest, France, [6]Nansen Environmental and Remote Sensing Center (NERSC), Bjerknes Center for Climate Research (BCCR), Bergen, Norway, [7]Department of Atmospheric and Oceanic Sciences, University of California, Los Angeles, Los Angeles, CA, USA, [8]Laboratoire d'Étude en Geophysique et Océanographie Spatiale, IRD, Toulouse, France, [9]Georges Lemaître Centre for Earth and Climate Research (TECLIM), Université catholique de Louvain, Earth and Life Institute, Louvain-la-Neuve, Belgium, [10]Institute of Marine Research (IMR), Bergen, Norway, [11]GEOMAR Helmholtz Centre for Ocean Research Kiel, Kiel, Germany, [12]Department of Oceanography, Dalhousie University, Halifax, NS, Canada

Key Points:

- The East Madagascar Current (EMC) retroflection is assessed. Evidence of EMC early retroflection is demonstrated for the first time
- Retroflection regimes are associated with EMC strength and mesoscale variability
- Knowledge of the EMC retroflection state helps understand regional ecosystem variability

Correspondence to:
J. D. Ramanantsoa,
oceanman1@live.fr

Citation:
Ramanantsoa, J. D., Penven, P., Raj, R. P., Renault, L., Ponsoni, L., Ostrowski, M., et al. (2021). Where and how the East Madagascar Current retroflection originates? *Journal of Geophysical Research: Oceans*, *126*, e2020JC016203. https://doi.org/10.1029/2020JC016203

Received 4 MAR 2020
Accepted 26 OCT 2021

Abstract The East Madagascar Current (EMC) is one of the western boundary currents of the South Indian Ocean. As such, it plays an important role in the climate system by transporting water and heat toward the pole and recirculating to the large-scale Indian Ocean through retroflection modes of its southern extension. Five cruise data sets and remote sensing data from different sensors are used to identify three states of the southern extension of the EMC: early retroflection, canonical retroflection, and no retroflection. Retroflections occur 47% of the time. EMC strength regulates the retroflection state, although impinged mesoscale eddies also contribute to retroflection formation. Early retroflection is linked with EMC volume transport. Anticyclonic eddies drifting from the central Indian Ocean to the coast favor early retroflection formation, anticyclonic eddies near the southern tip of Madagascar promote the generation of canonical retroflection, and no retroflection appears to be associated with a lower eddy kinetic energy (EKE). Knowledge of the EMC retroflection state could help predict (a) coastal upwelling south of Madagascar, (b) the southeastern Madagascar phytoplankton bloom, and (c) the formation of the South Indian Ocean Counter Current (SICC).

Plain Language Summary Using in situ and satellite observations, we show that the East Madagascar Current (EMC), a strong current flowing along the East Coast of Madagascar, often detaches from the coast before the southern tip of the island and goes directly into the Indian Ocean, the so-called EMC retroflection. The EMC retroflection is characterized by three well-defined forms: early retroflection, canonical retroflection, and no retroflection. The EMC Early Retroflection is an unusual abrupt return current straight to the Indian Ocean without reaching the detachment point, while the EMC Canonical Retroflection returns the mass flow in the vicinity of the southern tip of the island. No retroflection is characterized by the straight propagation of the flow toward the Agulhas Current. These three forms of retroflection are due to the strength of the EMC and the contribution of mesoscale eddies arriving from the Indian Ocean. Retroflections have implications for coastal upwelling strength, Southeast Madagascar phytoplankton bloom occurrences, and South Indian Ocean Counter Current (SICC) formation.

1. Introduction

Due to the presence of Madagascar Island and the consequence of wind-driven circulation in the South Indian Ocean, a continuous western boundary current, the East Madagascar Current (EMC), is formed along the east coast of the island (Lutjeharms et al., 1981; Penven, Lutjeharms, & Florenchie, 2006). The South Equatorial Current (Figure 1b) flows from east to west in the South Indian Ocean near the Mascarene Plateau (~60°E) between 10° and 20°S. It is mainly driven by southeasterly trade winds (Nauw et al., 2008; Palastanga et al., 2006). Upon reaching the western boundary of the east Madagascar coast, the South Equatorial Current bifurcates into the equatorward-flowing North Madagascar Current (Figure 1d)

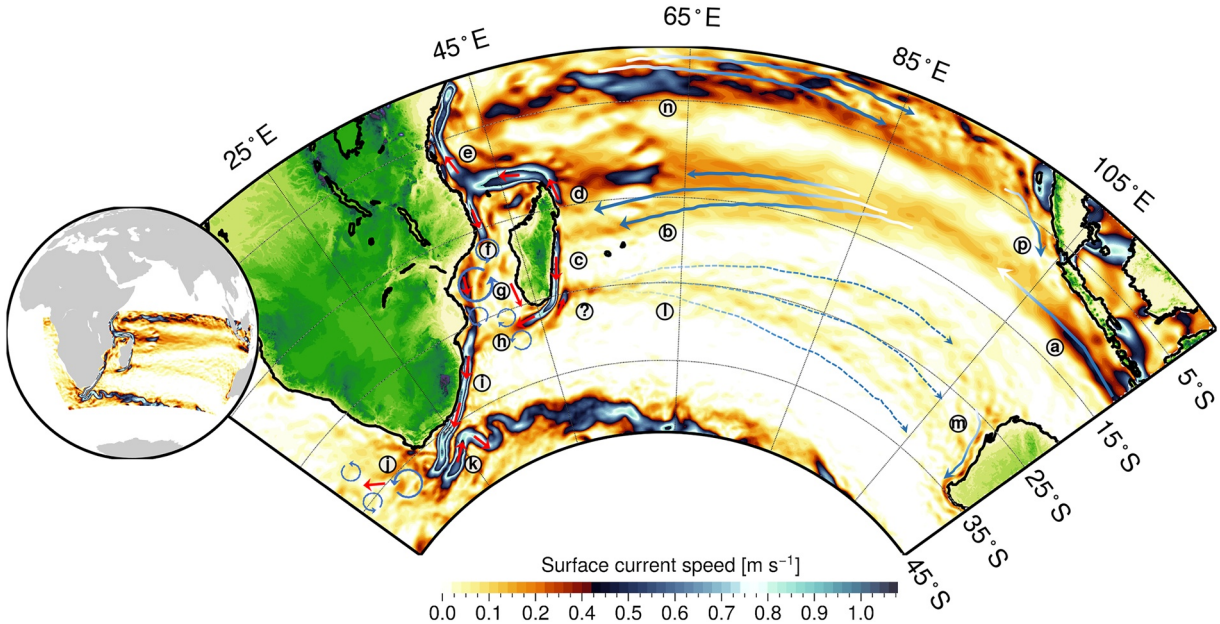

Figure 1. Schematic of the general ocean circulation in the South Indian Ocean. Schematic is built based on Wyrtki (1973); Lutjeharms (2006); Schott et al. (2009). Map shows South Indian Ocean currents features. The map shows mean surface geostrophic current from altimeter data and used for schematic illustration purposes only. Red arrows highlight coastal, western boundary currents, and their extensions. Plain blue arrows depict main offshore circulations. Dotted blue arrows illustrate non-permanent offshore circulation. (a) Indonesian Throughflow (IT) (Sprintall et al., 2009), (b) South Equatorial Current (SEC) (Chen et al., 2014), (c) East Madagascar Current (EMC) (Ponsoni et al., 2016), (d) North Madagascar Current (NMC) (Ponsoni, Aguiar-González, Nauw, et al., 2015), (e) East African Coastal Current (EACC) (Swallow et al., 1991), (f) Mozambique Channel anticyclonic eddies (Halo et al., 2014), (g) Southwest Madagascar Coastal Current (SMACC) (Ramanantsoa et al., 2018), (h) Dipole of eddies South of Madagascar (Ridderinkhof et al., 2013), (i) Agulhas Current (AC) (Lutjeharms, 2006), (j) Agulhas Rings (Olson & Evans, 1986), (k) Agulhas Return Current (ARC) (Lutjeharms & Van Ballegooyen, 1988), (l) South Indian Counter Current (SICC) (Menezes et al., 2016), (m) Leeuwin Current (LC) (Feng et al., 2009), (m) South Equatorial Counter Current (SECC) (Gordon et al., 1997), (n) South Java Current (SJC) (Sprintall et al., 1999). The question mark located southeast of Madagascar indicates the unclear circulation connecting the EMC (c) and the SICC (l) replicated from Menezes et al. (2014).

and poleward-flowing EMC (Figure 1c; Lutjeharms, 1976; Swallow et al., 1988). The South Equatorial Current bifurcation off the east Madagascar coast was documented to occur at approximately 17°S at the surface (Swallow et al., 1988) and at approximately 20°S at 800–900 m depth (Chapman et al., 2003). On average, the bifurcation of the southern branch of the South Equatorial Current takes place at 18°S, although Chen et al. (2014) observed an annual variability of approximately 1°, with the southernmost and northernmost bifurcation locations taking place in June-July and November-December, respectively.

The EMC originates from that southward branch resulting from the South Equatorial Current split after its separation near the east Madagascar continental margin. The EMC is a western boundary current flowing along the east coast of Madagascar and constitutes a major contributor to the Agulhas Current (Figure 1i; Penven, Lutjeharms, & Florenchie, 2006), which plays a significant role in the return flow of the Atlantic Meridional Overturning Circulation (Talley, 2013). Observational in situ data show that the EMC flows primarily over the eastern Madagascar continental slope, with a mean core placed at the surface and approximately 20 km off the coast, with a width ranging between 60 and 100 km (Ponsoni et al., 2016). Vertically, the EMC reaches an average depth of 1000 m, where there is a reversal of the flow that characterizes the transition to the equatorward-flowing East Madagascar Undercurrent (Ponsoni, Aguiar-González, Maas, et al., 2015). The EMC presents mean values of surface velocity on the order of 79 (±21) cm s^{-1} and 18.3 (±8.4) Sv volume transport. However, the current is marked by a well-defined nearly bimonthly variability (45–85 days), which leads to strong events with maximum velocities and volume transports of up to 170 cm s^{-1} and 50 Sv (Ponsoni et al., 2016). As shown by a combination of in situ and satellite observations, the nearly bimonthly variability explains approximately 41% of the EMC variance and is clearly forced by the arrival of westward-propagating sea level anomalies (Ponsoni et al., 2016). These anomalies might be perceived as mesoscale cyclonic and anticyclonic eddies. Upon arriving near the Madagascar coast, the eddies interact with the EMC, which is intensified (attenuated) by anticyclonic (cyclonic) features (Ponsoni

et al., 2016). The strength of the EMC also varies on interannual time scales, mostly related to the large-scale climate variability over the Indian Ocean. The large-scale sea surface height (SSH) signals, related to the occurrence of the Indian Ocean dipole (Saji et al., 1999), may interact with the Madagascar coast at a lag of +1 year after each Indian Ocean dipole phase. The positive phase of the Indian Ocean dipole is associated with positive SSH anomalies in the tropical Indian Ocean, which tend to decrease circulation in both tropical and northward extensions of the subtropical gyre. During negative phases of the Indian Ocean Dipole, an intensification of the EMC was observed, pointing to a strengthening and/or southward extension of the tropical gyre related to the Indian Ocean Dipole-induced negative SSH (Palastanga et al., 2006).

Before propagating toward the Agulhas Current, the southern extension of the EMC is also perceived to flow eastward and to act as a feeder of the South Indian Ocean Countercurrent (SICC; Figure 1l; Lutjeharms, 1988; Palastanga et al., 2006; Siedler et al., 2006). Pairing oceanographic cruise data and satellite observations, Lutjeharms et al. (1981) and Lutjeharms (1988) found that the southern extension of the EMC had a return current. Later, using satellite data and the OCCAM numerical model (Ocean Circulation and Climate Advanced Modeling; Gwilliam et al., 1997; Saunders et al., 1999), the concept of the EMC retroflection was reconsidered by Quartly et al. (2006). The sequences of satellite images agreed well with the model output, showing an intermittence of anticyclonic eddies moving westward, which seemed to affect the EMC retroflection. Siedler et al. (2009) demonstrated that the southern extension of the EMC has two states: the first is the state of no retroflection characterized by the flow directly contributing to the total volume transport of the Agulhas Current; and the second state is a retroflection where most of the flow returns back directly to the South Indian Ocean via the SICC. They found the existence of a variable retroflection with a significant proportion of the EMC flowing toward the Agulhas Current and almost half propagating into the SICC. Numerical models have difficulties simulating retroflection dynamics. In most modeling work in the region, based on ROMS (Regional Ocean Modeling System; Penven, Debreu, et al., 2006), HYCOM (Hybrid-Coordinate Ocean Model; Chassignet et al., 2007), HIM (Hallberg Isopycnal Model; Lambert et al., 2016), and NEMO (Nucleus for European Modeling of the Ocean), the location of the eastward-flowing SICC does not seem to correlate well compared to altimetry data. It is shifted 1–2° north, which cannot accurately simulate the dynamics of the retroflection (see Figure 4 in Lambert et al., 2016; Figure 5 in Siedler et al., 2009; Figure 2 in Halo et al., 2014). Halo et al. (2014) and Jose et al. (2016) simulated eddy activities south of Mozambique and southwest of Madagascar. Both simulations explained the complex role of mesoscale eddy processes driving offshore propagation of water from the EMC through the dipole of eddies south of Madagascar.

The characteristics of retroflection and their mechanical drivers are still unknown. Few studies have accurately addressed the retroflection types or their formations. Siedler et al. (2009) suggested that the EMC holds two different modes, which change from one regime to the other, depending on the intensity of the EMC. The first mode is a westward flow after rounding the southern tip of Madagascar, which is induced by a cyclonic motion owing to friction with the inshore edge (de Ruijter et al., 2004). The second mode is an anticyclonic motion, owing to the southwestward flow of the EMC and hence to the absence of frictional effects with the slope. The planetary vorticity changes result in an anticyclonic motion to conserve absolute vorticity. This favors a retroflection to the east and northeast. Halo et al. (2014) indicated that the connection between the EMC and a retroflection could be established through the shedding of anticyclonic eddies, hence consistent with a non-persistent retroflection of the EMC, as stated by Quartly et al. (2006). de Ruijter et al. (2004), and Palastanga et al. (2007) added that the interactions of the westward-propagating mesoscale eddies drifted from the Indian Ocean between 20° and 30°S with the mean flow of the EMC appearing to initiate the formation of a retroflection. However, Ou and De Ruijter (1986) and Arruda et al. (2014) were the few studies suggesting a theoretical explanation of the retroflection in the South Indian Ocean. Ou and De Ruijter (1986) investigated the key processes responsible for the Agulhas Current retroflection. Using one- and half-layer models, they explained the formation of a meander initiating retroflection due to the interaction between the Agulhas Current intensity and the continental margin. Arruda et al. (2014) suggested that the increase of the basic eddy volume associated with variation of β-effect and the net mass flux going into the eddies explained the Agulhas Current retroflection dynamics from an analytical model satisfying the mass conservation, the momentum balance, and the time-dependent equation. Both studies converge to suggest that potential vorticity balance variation is associated with the generation of retroflection for the Agulhas Current case, which may also be replicated for the EMC case.

EMC retroflection has recently gained interest in the scientific community because of its possible link with the Southeast Madagascar Bloom (Dilmahamod et al., 2019), with coastal upwelling in southern Madagascar (Ramanantsoa et al., 2018), and its influence on Agulhas Current variability (Lutjeharms et al., 1981). Previous studies have documented that EMC retroflection transports nutrient-rich waters, triggering this massive phytoplankton bloom to expand toward the central Indian Ocean (Longhurst, 2001; Raj et al., 2010). The EMC southern extension behavior is also known to influence coastal upwelling at the southern tip of Madagascar (Ho et al., 2004; Ramanantsoa et al., 2018), which has implications for local biological productivity (Bemiasa, 2009). The impact of the retroflection on coastal upwelling and on the transport of nutrients into the region of the bloom is unknown.

The Indian Ocean has recently been described as the fastest-warming ocean in the world for the last two decades (Hu & Fedorov, 2019; Rao et al., 2012). The western boundary currents in this ocean, such as the EMC, play a key role in transporting heat from the tropics toward the poles (Deo et al., 2011; Hastenrath, 2000; Sheppard, 2003). In that case, the EMC is a central location connecting the Agulhas Current and the central Indian Ocean. There is a crucial need to assess the functioning of the EMC to successfully establish the connection between tropical and/or subtropical latitude water and the Agulhas Current. Knowledge of the EMC retroflection variability will be key to understanding the variability of the Agulhas Current and the recirculation in the southwest Indian Ocean. The disruptions of anticyclonic eddy pulses south of Madagascar due to retroflection (Siedler et al., 2009) may induce sensitivity in the Agulhas Current System since mesoscale activities are the major source of Agulhas Current water (de Ruijter et al., 2004; Penven, Lutjeharms, & Florenchie, 2006). This may have an impact on the magnitude of the Agulhas Current leakage (Figure 1j; Beal et al., 2011), which regulates the exchanges between the Indian and the Atlantic Oceans (Talley, 2013).

On the other hand, the EMC is also connected with the SICC (Menezes et al., 2016). The SICC is a shallow permanent current flowing from Madagascar to western Australia between the latitudes of 20° and 30°S. The SICC flows in the opposite direction of the classical theories of wind-driven circulation (Menezes & Vianna, 2019) and is associated with a jet of salinity front and a subsurface thermal front in the central Indian Ocean (Siedler et al., 2006; Palastanga et al., 2007), important for salt and heat distribution in the Indian Ocean region. However, the link between the EMC and the SICC is still not well defined to understand the advection of nutrient-rich from the east coast of Madagascar favoring the formation of the Madagascar southeast phytoplankton bloom.

Very few studies have addressed the southern extension of the EMC, resulting in the lack of an exact definition of the EMC retroflection concept. Using multisensor satellite and in situ cruise data, this study intends to describe the characteristics of the EMC retroflection and determine the associated dynamic processes and the local and regional impacts.

2. Data and Methods

2.1. In-Situ Data

A compilation of vessel-mounted acoustic Doppler current profiler (VMADCP) measurements was collected during five different research cruises operated around the EMC retroflection region. Explicit details of cruise data are given in Table 1. VMADCP data operated by German research cruises were collected from the Data Publisher for Earth and Environmental Science (PANGAEA: https://www.pangaea.de/). The two remaining VMADCPs were obtained from the Institute Marine Research (IMR) database. Data were already processed by their respective institution's holder. VMADCP data are used to highlight the structure of the EMC at 25°S. Data are cropped only at the retroflection zone. Velocity components will be used to characterize the horizontal and vertical structure of captured retroflections.

A 2.5-year (October 2010 to February 2013) time series of EMC volume transport (Ponsoni et al., 2016) from a combination of several mounted acoustic Doppler current profilers (ADCPs) and recording current meters (RCMs) deployed at 23°S are used to measure the link between the daily volume transport of the EMC and the characteristics of its associated retroflection. To inspect the relationship between the EMC strength and its retroflection characteristics, we make use of a daily 2.5-year time series of the EMC volume transport estimated from in situ data. This time series spans from October 2010 to February 2013 and was provided by five vertical moorings deployed in a cross-shore transect at ~23°S, with the most inshore

Table 1
Description of Vessel Mounted Acoustic Doppler Current Profiler (VMADCP) Data Sets Used in the Study With Their Associated Periods, Vessels and Research Cruises

VMADCP	Code	Vessel	Cruise name	Date	Doi
Figure 2a	199	RSS Discovery Survey	GEOMAR 1987	30-01-1987/21-02-1987	10.1594/PANGAEA.319631
Figure 2b	180	R.V. Knorr	GEOMAR 1995	11-06-1995/11-07-1995	10.1594/PANGAEA.319573
Figure 2c	300	R.V. Fridtjof Nansen	ASCLME 2008	01-09-2008/07-09-2008	–
Figure 2d	–	R.V. Meteor	M100-2	10-2013/21-10-2013	–
Figure 2e	–	R.V. Fridtjof Nansen	Nansen 2018	28-10-2018/02-11-2018	–

Note. The state of the availability of the VMADCP data on Figures 2c–2e are in the process of being published by their respective institution holder.

and offshore moorings placed at distances of approximately 6 and 110 km from the coast, respectively. To provide detailed information on the vertical velocity and velocity shear structure at depths in which the EMC is stronger, each mooring line was equipped with an upward-looking ADCP installed at a depth of approximately 500 m. Additionally, other ADCPs and RCMs were strategically deployed at different depths depending on the mooring line. A sketch of the mooring lines and their respective instruments is shown in Ponsoni et al. (2016; in their Figure 2a). As described by these authors, by time synchronizing the data sampled with all instruments, it was possible to determine the alongshore velocities passing through the cross-shore transect from the seafloor to the surface to provide an accurate estimation of the EMC volume transport. For a complete description of the methodology used for the data processing and volume transport computation, the reader is referred to Ponsoni et al. (2016) (in their Section 2).

We use quality-controlled surface drifter data from the Global Drifter Program (Lumpkin & Pazos, 2007). The data spanned from February 1979 through June 2020. Data have global coverage within more than 85% of the ocean surface (Maximenko et al., 2012). The drifters have a battery life of up to 5 years, and the post-processed data yield geolocations of the buoys every 6 hr (Lumpkin et al., 2012). Drifters are advected with near-surface flow (Lumpkin et al., 2012; Niiler, 2001). These can be used to study the direction and follow trajectories of ocean currents, such as retroflection. All available surface drift trajectories passing in the EMC region are collected from the Global Drifter Program database (Global Drifter; https://www.aoml.noaa.gov/phod/gdp/interpolated/data/subset.php). This selects drifter trajectories targeting the fate of the EMC southern extension, thus with a retroflection or not.

2.2. Satellite Data

Altimetric SSH data were collected from the Copernicus Marine and Environment Monitoring Service (CMEMS; http://marine.copernicus.eu). The delayed-time data set is a merged product from multiple altimeters (Ducet et al., 2000) and is available on a 0.25° horizontal grid resolution as daily outputs from 1993 until the present. The SSH product is the global ocean gridded L4 SSH and derived variables reprocessed, collected from (Copernicus; http://marine.copernicus.eu/services-portfolio/access-to-products/?option=com_csw&view=details&product_id=SEALEVEL_GLO_PHY_L4_REP_OBSERVATIONS_008_047). Velocity field data are retrieved from the global total surface and 15 m current (Copernicus-Globcurrent) from altimetric geostrophic currents and modeled Ekman current reprocessing (https://marine.copernicus.eu/services-portfolio/access-to-products/?option=com_csw&view=details&product_id=MULTIOBS_GLO_PHY_REP_015_004). Data are used to derive the estimated geostrophic velocity of EMC and to detect the retroflection spatial extent for the period 1993–2017.

The surface current products are obtained from the GlobCurrent project (Johannessen et al., 2016; http://www.globcurrent.org). Based on multisatellite altimetry data from 1993 to 2015, daily estimates of surface geostrophic currents are provided at a spatial resolution of 25 km. Three-hourly Ekman currents (at the surface and 15 m depth) are estimated from Argo floats, surface drifter and near-surface winds, and combined with the velocity data. They are combined as monthly composites for this study. More details on how GlobCurrent data are produced and their limitations can be found in Rio and Santoleri (2018), Feng et al. (2018), and Cancet et al. (2019).

The Optimum Interpolation Sea Surface Temperature (OISST) products version 2.1 are used to measure the surface signature of the coastal upwelling south of Madagascar (Reynolds et al., 2007). SST products were obtained from the National Centers for Environmental Information (NOAA; https://www.ncdc.noaa.gov/oisst). SST has a spatial grid resolution of 0.25° and a monthly temporal resolution.

Monthly chlorophyll-a concentration data were obtained from the MODIS chlorophyll-a level 3 (MODIS; http://oceancolor.gsfc.nasa.gov/cgi/l3) 4 km resolution grid, covering the period of 2002–2017. Chlorophyll concentration is used to characterize the response of the southeast Madagascar phytoplankton bloom to early retroflection.

2.3. Retroflection Tracking

The EMC retroflection is identified from altimetry by selecting a specific SSH contour as a streamline representative of the EMC path. The selected contour is chosen as the mean sea level in the EMC southern extension region (42°–50°E and 22°–28°S), over a bathymetry ranging from 200 to 2,000 m, and with current speeds higher than 35 cm s^{-1}. The westernmost contour position determines the EMC retroflection location. This methodology is equivalent to the one applied to the Agulhas current by Backeberg et al. (2012), Loveday et al. (2014), and Renault et al. (2017).

2.4. K-Mean Clustering

The unsupervised *K*-mean clustering method is applied to define the spatial distribution of the EMC retroflection turning points over time. *K*-means clustering is an unsupervised classification approach usually used to define undetected patterns in data (Hartigan & Wong, 1979). The classification method assigns samples, each data point, to belong to an identified k class. Classes are defined according to the density of partitioned data. A point is determined to belong to a cluster based on a calculation of its Euclidian distance metric from a cluster center called the barycenter (Ye et al., 2007; Singh et al., 2013). The barycenters are placed at a minimum distance possible to the optimal classified points. The assigned group is identified according to their minimum classic Euclidian distance metric of the detected EMC retroflection positioning expressed here as $Dist(x_i, y_i) = \sqrt{\sum_{i=1}^{n} (x_i - c_x)^2 + (y_i - c_y)^2}$ where Dist is the Euclidean distance metric between barycentre c and n samples. (x_1, x_2, ..., x_n) and (y_1, y_2, ..., y_n) are samples coordinates. (c_x, c_y) is the barycentre spatial positioning (AbdAllah & Shimshoni, 2016; Singh et al., 2013).

Two instances of classification are performed to maximize the efficiency of the classification applied to a large data dispersion (White et al., 2010). The first instance consists of separating the data into two main classes: the retroflection class and the no retroflection class. The second instance afterward focuses on classifying the retroflection class into two new classes. This approach is applied to obtain precision on the retroflection class distribution and the lowest standard deviation of the spatial distribution.

2.5. Mesoscale Eddy Activity

Altimetry gridded data are used to generate monthly vorticity and monthly eddy kinetic energy (EKE) for the period 1993 to 2017. Vorticity is performed to identify potential rotative circulation in the retroflection areas, expressed as follows: $\zeta = \frac{\partial v}{\partial x} - \frac{\partial u}{\partial y}$, where v and u are the meridional and zonal surface velocities (Ridderinkhof et al., 2013). The EKE is computed to quantitatively examine the signature of mesoscale eddy activities in the retroflection areas. EKE is calculated by using $\frac{1}{2}(u'^2 + v'^2)$ (Jia et al., 2011), where u' and v' are the zonal and meridional geostrophic velocity anomalies, respectively.

The barotropic energy conversion rate quantifies the transfer of momentum between the mean flow and mesoscale eddy activities (Ma & Wang, 2014). In this study, the barotropic energy conversion rate is calculated to evaluate the energy exchanged between the impinged eddies arriving from the central Indian Ocean (de Ruijter et al., 2004; Quartly et al., 2006) and the EMC. The barotropic energy conversion rate is expressed as follows (Raj et al., 2016):

$$Br = -\overline{u'u'}\frac{\partial \bar{u}}{\partial x} - \overline{u'v'}\frac{\partial \bar{u}}{\partial y} - \overline{u'v'}\frac{\partial \bar{v}}{\partial x} - \overline{v'v'}\frac{\partial \bar{v}}{\partial y} \quad (1)$$

u' and v' are zonal and meridional geostrophic velocity anomalies, respectively. u and v are the surface geostrophic current velocities. The monthly gridded altimeter satellite product explained in Section 2.2 was used to determine the barotropic energy conversion rate. The positive values of Br indicate a transfer of energy from the mean flow to the eddy field, while negative values imply energy transfer from the eddy field to the mean flow (Ma & Wang, 2014; Raj et al., 2016).

2.6. Eddy Tracking Algorithm

Automatic eddy-tracked data derived from multimission altimetry eddy trajectories are used to estimate eddy characteristics and trajectories in the retroflection area. Mesoscale eddy locations and trajectories in the retroflection area were obtained from the fourth release of an existing eddy global data set (Chelton et al., 2011). It is an automated eddy algorithm that tracks eddies from daily SSHs (on a 0.25° Cartesian grid), derived from the delayed-time "two-sat merged" product of archiving, validation, and interpretation of satellite oceanographic data (AVISO). The eddies are detected from a "growing method" (Schlax & Chelton, 2016), starting with identifying individual SSH extrema (negative for cyclones and positive for anticyclones) and locating all neighboring pixels with SSH values lying above a sequence of thresholds. When a set of connected pixels satisfies a set of criteria used to define coherent and compact structures, an eddy is defined. The tracking of eddies is then performed by pairing eddy structures that are within allowable ranges of distance, radius and amplitude of the initial eddy at subsequent time steps. These global mesoscale eddy trajectory products (Delepoulle et al., 2018) are obtained directly from the AVISO website (http://www.aviso.oceanobs.com/duacs/).

2.7. Virtual Particles Simulation

A Lagrangian experiment is applied to demonstrate the capacity of early retroflection rerouting particles offshore east of Madagascar. Virtual particles were seeded in the core of the EMC, a one-degree grid poleward from the SEC bifurcation position (~18°S) (Chen et al., 2014), at the following coordinates of 50°E and 18°S. Particles were advected forward in time using daily altimetry-derived surface current and surface meridional and zonal velocity components from the gridded altimetry data (Liu et al., 2014).

3. Results

3.1. Hydrographic Observation of the EMC Southern Extension Characteristics

Figure 2 illustrates a series of captured sea surface velocities and sections of meridional velocity recorded from VMADCP data. SSH from gridded altimetry data at the same period of the recorded data are added to follow the pattern of circulation seen in the VMADCP. VMADCP data reveal the horizontal structure of the EMC, characterized by a narrow poleward jet, close to the shelf break around 25°S, with an averaged core velocity of 45 cm s^{-1} (Figures 2a–2e). On the eastern side of the EMC at 25°S, an opposite flow is observed, ~160 km from the coast, with an average velocity of 40 cm s^{-1} (Figures 2a–2e), consistent with Nauw et al. (2008).

All sections present opposite meridional velocities between the EMC and the return flow (Figures 2a–2e). However, while the EMC meridional velocity is consistently intense beyond a depth of ~250 m, the return flow starts to weaken below 100 m (Figures 2f–2j). Small differences in surface velocities and significant differences in meridional velocities at depth could be indicative of eddy-mean flow interactions when anticyclonic eddies shallower than the EMC approach the Madagascar coast near 24°S. Eddy-EMC interactions may induce a transfer of momentum toward the mean flow (Halo et al., 2014). Nauw et al. (2006) also reported an anticyclonic shear close to the core of EMC in the observed vertical transect from VMADCP at 25°S (see their Figure 5a).

Altimeter SSH is overlaid on top of VMADCP surface velocities. Good agreement is found between both data sets (Figures 1b–1e). A high value of SSH (> 140 cm) delineates circular features indicative of anticyclonic

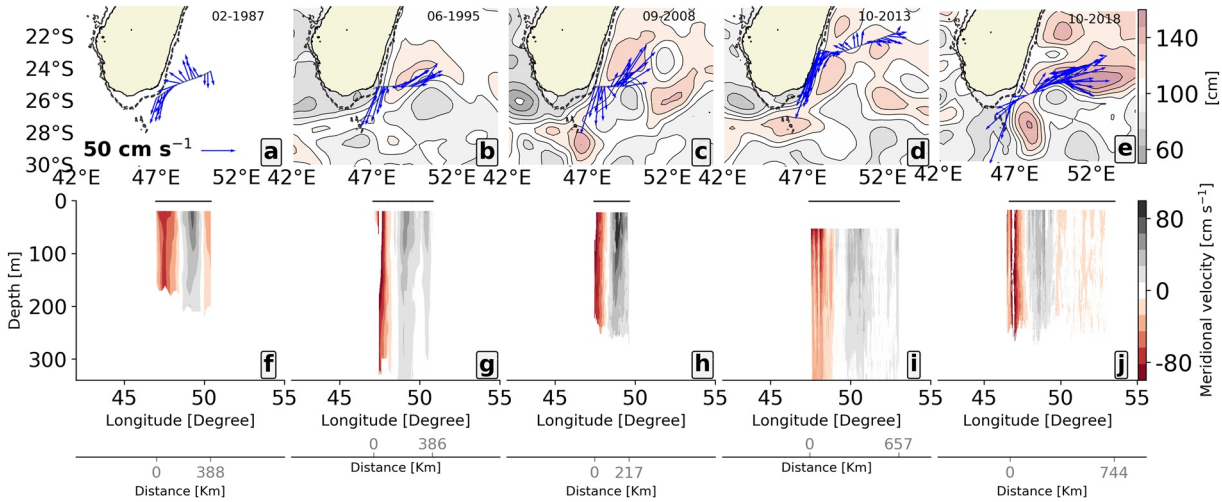

Figure 2. Hydrographic tracking of the EMC retroflection at ~25°S. Panels (a)–(e) are transects showing the horizontal structure of the current. Arrows represent directions and intensities of the near surface flow (~20 m). Gray lines, in which arrows originate, indicate the selected vessel trajectories. Overlapping maps show weekly SSH according to each VMADCP measurement period (bottom). Note that satellite altimetry data were not available during the 1987 cruise for the first panel (a). Black horizontal lines at 0 m present the measured distance scale of each transect. Panels (f)–(j) illustrate the vertical structure of the EMC southern extension measured at the same location from the VMADCP. The current vectors along each transect are projected onto the longitude axis, and their distances from the coast are measured from the closest coastline location.

eddies, a similar approach used in Ridderinkhof et al. (2013). VMADCP surface velocity captured anticlockwise rotative flow occurring at the edge of the high SSH approaching the continental shelf (Figures 2b–2e). Several studies (Anggoro, 2017; de Ruijter et al., 2004; Ridderinkhof et al., 2013; Ternon et al., 2014; Quartly et al., 2006) have used observations of sea level heights to identify ocean circulation patterns and eddy features. Sea level anomaly products are frequently used to characterize mesoscale eddy behaviors and characteristics; however, many studies have also applied SSH to identify and track the presence of mesoscale eddies (Laxenaire et al., 2020; Ridderinkhof et al., 2013). Thus, Figures 2b–2e show patterns of anticyclonic eddies drifting between 22° and 24°S from the Indian Ocean to the Madagascar coastline, in agreement with Quartly et al. (2006) and Dilmahamod et al. (2018). The anticyclonic eddies appear to merge or disintegrate in the EMC around 25°S.

SSH maps, using the gridded altimetry product, shown in Figures 2b–2e are reillustrated in Figures 3a–3d in a larger domain. The retroflection tracking positioning explained in Section 2.3 is applied to the enlarged SSH maps. Retroflection positioning, indicated by blue stars, is identified during the same period of the collected VMADCP: Figures 3a and 3c detect retroflections further downstream in the Agulhas Current region, which is indicative of no EMC retroflection, while Figures 3b and 3d show retroflections in the southern extension of EMC. Interestingly, while Figure 3b reveals a retroflection beyond the southern tip of Madagascar, Figure 3d shows the presence of a retroflection prematurely formed along the southeast coast of the island. This retroflection appears to start farther upstream, in the vicinity of 25°S, before progressing downstream.

3.2. Three States of Retroflection Extent

Figure 4 depicts trajectories of available drifters passing inside the EMC core illustrated by the red rectangle from February 1979 to June 2018. Nineteen drifters followed an early retroflection of the EMC (Figure 4a). Another 11 drifters follow the retroflection around the southern tip of the island (Figure 4b). Finally, 18 drifters joined the Agulhas Current, exhibiting no retroflection (Figure 4c). On average, drifters take a few months to 1 year to travel from the EMC box to the east off 60°E during a premature retroflection event at 25°S (Figure 4a). Some drifters, which return back to the Indian Ocean further south, take approximately one year and a half to reach the offshore east of the island. In the no retroflection case, drifters travel two to three years to delineate the subtropical early gyre in the Southwest Indian Ocean (Figure 4c). A list of all drifters and a statistical summary are presented in Table 2. Drifter trajectories basically reached

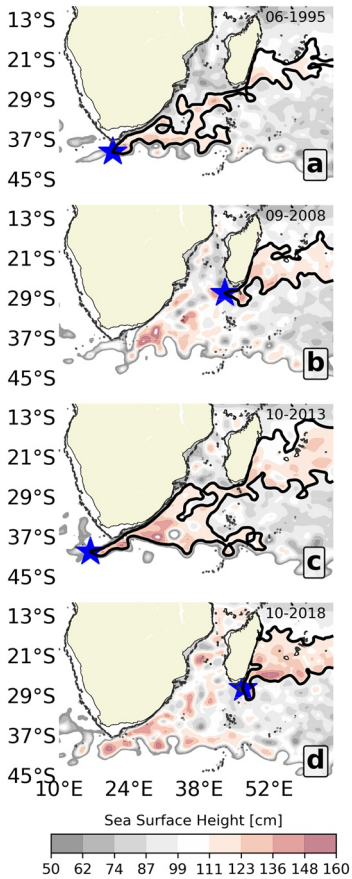

Figure 3. Altimeter satellite-based EMC retroflection tracking. Panels (a)–(d) illustrate the EMC retroflection position detection. Black lines are the detected SSH contours performed to track the EMC extension. Blue stars highlight the westernmost point of the contour, considered the EMC retroflection position. Maps are the enlarged views of SSH maps seen Figures 2b–2e.

opposite locations, where 37.5% of drifters joined the Agulhas Current, while 62.4% of the remaining drifters returned back to the Indian Ocean through retroflection.

Monthly EMC retroflection positions are detected from the gridded satellite altimetry over the 1993 to 2017 period. The retroflection position is the westernmost of the selected SSH contour satisfying the conditions explained in Section 2.3 to encompass the EMC flow. Figures 5a–5c show the mean position of the EMC retroflection for each retroflection mode (red stars). These are generated by averaging the satellite data (see contours and isoline of SSH) of the composite for each retroflection type. Figure 5d highlights the spatial distribution of the EMC retroflection partitioned using the *k*-mean clustering method, assuming the existence of three classes. Each classified retroflection position is combined to build, according to retroflection types, the mean position composite mentioned in Figures 5a–5c. The three distinct cases of EMC retroflection obtained are early retroflection, canonical retroflection, and no retroflection. Both drifter trajectories (Figures 4a–4c) and satellite data (Figures 5a–5c) confirm the presence of three EMC retroflection case scenarios. On monthly timescales during the period 1993 to 2017, an EMC retroflection is identified over 47% of events (early retroflection: 13%; canonical retroflection: 34%). The 53% remaining correspond to the case when the flow does not retroflect and propagates straight into the Agulhas system. This is in line with the findings of Siedler et al. (2009) with the addition of the early retroflection case as a new state of the EMC.

The EMC early retroflection is the upstream eastward drift of EMC from the east coast of Madagascar. The highest longitudinal probability of the early retroflection position is at 47.6°E ± 0.41, while it is at 43.8°E ± 1.8 for the canonical retroflection (Figure 5b). Early retroflection latitudinal average positioning is 25.65°S (Figure 5f). Table 3 summarizes the occurrence and position of the retroflection types.

3.3. Description of Early Retroflection Events

To address the drivers of early retroflection events, we use an integrated EMC volume transport time series collected from ADCPs and RCMs combined data (Ponsoni et al., 2016). In addition, EMC geostrophic velocity, provided by the gridded altimetry data, is retrieved from the nearest location of the moored ADCPs. On daily time scales, a significant linear relationship, a correlation coefficient factor of 0.61 at a 95% confidence level, is found between the two time series, which are the southward volume transport and the surface geostrophic velocity of the EMC (Figures 6a and 6b).

The daily EMC retroflection position is tracked over the period coinciding with the ADCP deployment from October 1, 2010 to February 1, 2013. The results reveal that the occurrences of early retroflections coincide with intense southward EMC volume transport (Figures 6a and 6c). During the time period of October 11, 2010 to April 1, 2013, early retroflection positions persisted for an average of 15 days, depending on the number of occurrences. An early retroflection is also found to persist over 2 months (December 2010 to January 2011) when the southward EMC volume transport peaked at 45 Sverdrup (*Sv*) (1 $Sv = 10^6$ m^3 s^{-1}), while it did not occur for four consecutive months (March 2012 to June 2012) when the transport is ~18 *Sv*, which is the average transport of the EMC at this latitude (Ponsoni et al., 2016; Ramanantsoa, 2018). In summary, the likelihood of early retroflection increases with the volume of EMC transport and drops when the volume transport is low.

Time periods with intense volume transport (above one standard deviation) are used to construct composite means of SSH and ocean color. Figures 7a and 7b presents characteristics of an early retroflection at 24.5°S.

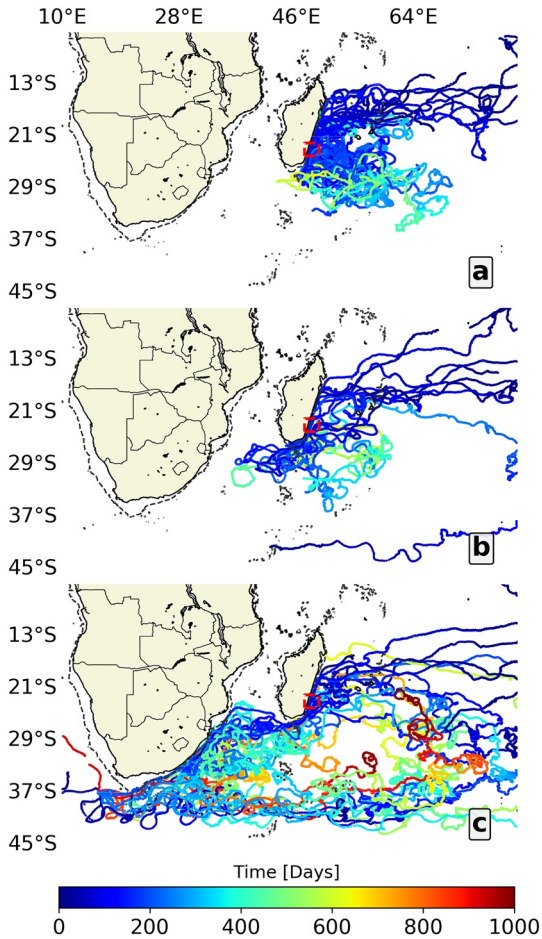

Figure 4. EMC retroflection spatial extent based on the global surface drifter data set. Panels (a)–(c) present trajectories and time durations of surface drifter floats depicting the three cases of EMC retroflection. (a) Selected surface drifters that follow the EMC early retroflection case. (b) Drifters that depict the EMC canonical retroflection. (c) Combined drifters that represent the EMC no retroflection case.

This link between high volume transports and earlier retroflections is consistent with the results of previous theoretical work in the Agulhas system (Ou & De Ruijter, 1986), suggesting that the interaction between coastline curvature and high transport of the Agulhas Current tends to favor early retroflection. This finding is reinforced by Arruda et al. (2014). These authors have shown that variations in the Rossby number of deformation seem to induce inertial and momentum imbalances of the Agulhas Current and, as consequence, generate an upstream retroflection (the so-called Agulhas Current early retroflection). Figure 7a shows that the EMC early retroflection appears to originate from 24.5°S (black star) and that the EMC flow seems to drift eastward following a zonal band at ~25.5°S. A high value of SSH is observed in that position, indicative of an anticyclonic rotation, which seems to be responsible for the early eastward drift at this latitude. This is also seen in Figure 7c, which depicts intense positive vorticity over a wide range, indicative of anticyclonic circulation along the east coast but not necessarily anticyclonic eddies. However, mesoscale anticyclonic eddies are known to drift from the central Indian Ocean and propagate into the EMC (de Ruijter et al., 2004; Dilmahamod et al., 2018). Accordingly, the wide range of positive vorticity could be the signature of the anticyclonic presence. Hence, the arrival of anticyclonic eddies increases the EMC strength, which is in line with Ponsoni et al. (2016), and induces an abrupt detachment of the flow from the coast. The intense volume transport of the EMC (Figure 6a) together with the contribution of mesoscale eddies promotes early retroflection occurrences (Figure 7a). In addition, the early detachment of the EMC also presents a signature in chlorophyll-a extending from the upwelling south of Madagascar (Ramanantsoa et al., 2018) to more than 2° longitude offshore toward the east (Figure 7b). This shows that early retroflection can trigger phytoplankton bloom patches, usually occurring in this region, as suggested by Dilmahamod et al. (2019).

Two synoptic developments of the EMC early retroflection from the onset to the full formation are illustrated in Figures 8 and 9. These figures intend to demonstrate a synoptic preformation of early retroflection associated with an anticyclonic eddy using the automatic eddy-tracked data explained in the data section, propagating from the Indian Ocean toward the south of Madagascar. Propagations of high sea level agree well with the westward movement of anticyclonic eddies reaching the edge of the

Table 2
Summary of Available Global Drifters Showing Three Types of EMC Retroflection

	EMC early retroflection	EMC canonical retroflection	EMC No retroflection
Percentage	39.5%	22.9%	37.5%
Period	few months to 1 year	~1.5 years	2–3 years
Drifter N°	20,333; 34,157; 37,631; 41,243	25,020; 26,219; 83,341; 114,826	43,580; 44,296; 54,395; 63,875
	41,337; 41,339; 42,539	2,134,150; 9,729,754; 9,730,550	70,942; 70,957; 70,969
	70,963; 71,090; 81,834	61,479,400; 63,043,010; 63,897,000	70,970; 81,849; 83,446
	88,664; 90,502; 109,538	63,941,920	115,991; 126,948; 127,314
	109,539; 133,655; 9,421,901		127,353; 2,134,164; 9,619,819
	9,730,550; 63,040,060; 6,482,637		60,609,830; 60,750,130

Note. Table summarizes the drifters for each retroflection type, the period of traveling from the EMC to the central Indian Ocean, and the identity number of drifters.

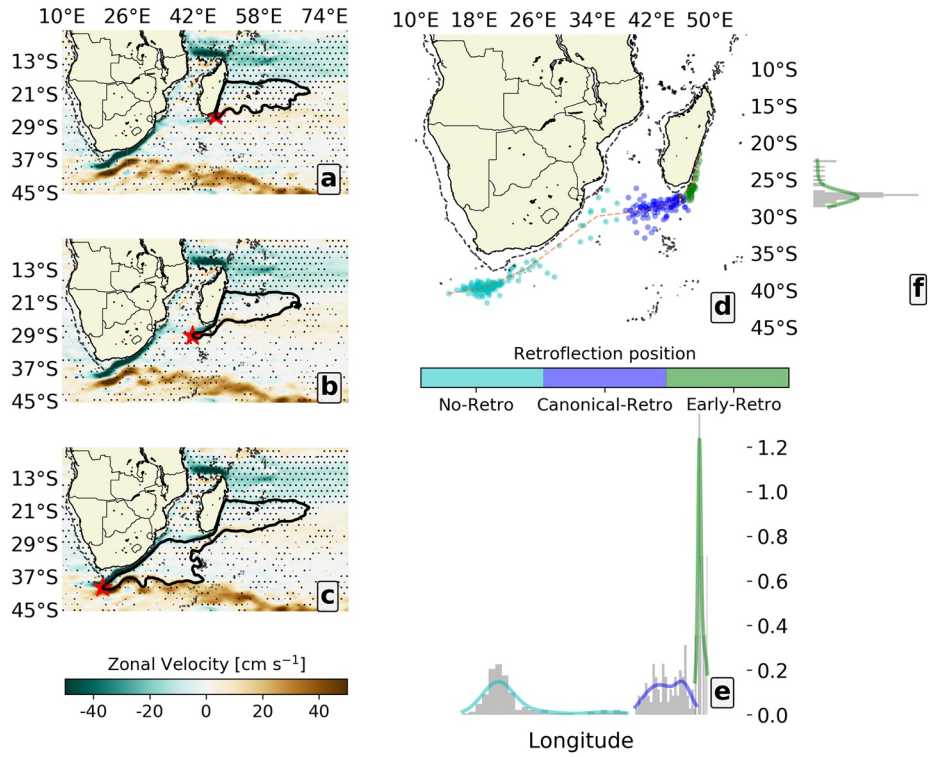

Figure 5. EMC retroflection spatial extent based on satellite altimeters. Panels (a)–(c) display composites of detected EMC retroflection positions using the SSH from satellite altimetry. The black contour represents the EMC and its retroflection. Red stars highlight the westernmost point of the selected SSH contour, considered as the EMC retroflection position. The maps in the background represent composites of zonal velocity corresponding to each retroflection case. Hatched black dots indicate a 95% confidence level according to a two-tailed Student's *t*-test. Panel (d) presents the spatial classification of the EMC retroflection position from the unsupervised k-mean clustering. The dotted red line delineates the most likely location of EMC retroflection positions. Each classified EMC retroflection case is used to build the composites of panels (a)–(c). Panel (e) displays the longitudinal distributions of the three EMC retroflection cases. Panel (f) displays the latitudinal distribution for the early retroflection case.

EMC. An anticyclonic eddy seems to trigger the eastward veering of the EMC. It enhances the flow to consequently form an early retroflection. Although it is difficult to provide a detailed explanation of how the anticyclonic eddy detaches the core of the EMC to drift eastward, Figure 8 illustrates only the altimetric observation of the early retroflection formation from a synoptic development perspective. Figure 9 also shows a similar process, while it shows the eventual shift from a canonical retroflection case to an early retroflection case. This confirms the progressive arrival of high SSHs reaching 160 cm (in line with Figure 2), overlapping with anticyclonic eddy tracking. It also reinforces the link between the preformation of an early retroflection and the association with anticyclonic eddies. Virtual particles were released in the EMC core to coincide with the synoptic early retroflection period. This emphasizes the argument that the early

Table 3
Statistical Summary of Retroflection

	Early retroflection	Canonical retroflection	No retroflection
Occurrences	13%	34%	53%
Lon. mean position	47.6 ± 0.41	43.8 ± 1.8	19.1 ± 5.37
Lat. mean position	25.6 ± 1.2	28.1 ± 0.4	40.1 ± 2.12
Skewness	2.57 (Lat. position)	−1.29 (Lon. position)	3.74 (Lon. position)

Note. Lon. is longitudinal, while Lat. is latitudinal direction. Skewness measures dispersion of the variation to test if it is distributed more to the left (negative) or to the right (positive) of the average.

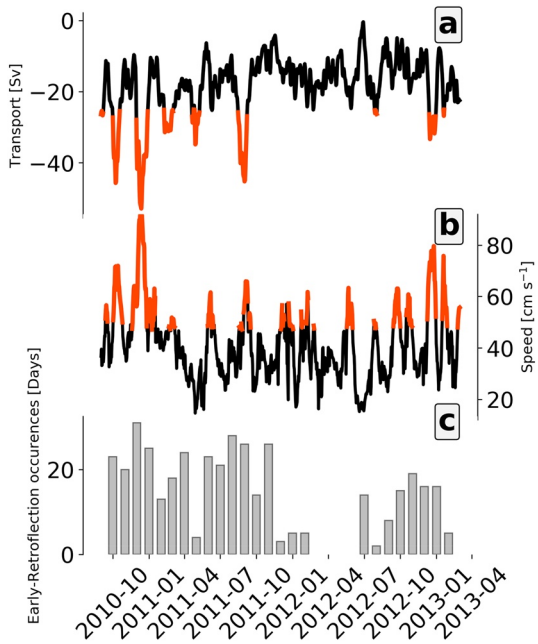

Figure 6. Evidence of the EMC early retroflection. (a) Time series of EMC northward volume transport from ADCP (Ponsoni et al., 2016). (b) Time series of the surface geostrophic currents from the satellite altimetry data at the same location (~23°S). EMC current speeds and volume transports higher than the standard deviation are highlighted in red. (c) Monthly EMC early retroflection occurrences computed from the detection algorithm.

retroflection triggers a premature eastward transport of water and is responsible for the advection of EMC water parcels and perhaps nutrients toward the center of the Indian Ocean.

3.4. Dynamical Processes

Figures 10 and 11 demonstrate the dual roles of the EMC strength and the mesoscale activities defining the type of retroflection. Figure 10 presents the occurrences of retroflection cases, the EMC surface geostrophic velocity anomalies, and the surface EKE for the period 1993–2017. Occurrences of retroflection cases are highlighted by red-shaded bands for the early retroflection, while blue-shaded bands depict canonical retroflection over the period of the study. Moreover, blank spaces in between account for the period of no retroflection events. Time series: (a) Gray time series is the monthly anomaly of the EMC surface current speed, generated from the gridded satellite altimetry, already used in Figure 6b, and (b) green and blue time series are the EKE extracted from early- and canonical retroflection areas, respectively. These areas are illustrated by rectangles in Figures 11a and 11b. The computation of the EKE is explained in Section 2.5.

Figures 11a–11c show the EKE mean composite of each retroflection type, similarly performed as in Figures 5a–5c. Figures 11d–11f show the results of the mean composite characterized by both EMC current strength and EKE intensity variations highlighted in Figure 10. Figure 11d is the mean composite of SSH associated with anomalously high EMC surface speeds (above one standard deviation), extracted near the ADCP mooring location, and anomalously high EKE extracted from the early retroflection area (above one standard deviation in the green box in Figure 11a). The mean composite of each retroflection type is then assessed. In agreement with the previous section, it corresponds to an early retroflection. Positive abnormally high EMC speeds tend to promote early retroflection. Moreover, anticyclonic eddies from the Indian Ocean also induce an enhancement in EMC speeds and promote an early eastward drift of the EMC southern extension in the vicinity of ~25°S. The synoptic development illustrated in Figure 8 has confirmed the involvement of anticyclonic eddies triggering early retroflection, and the retroflection mode can be shifted from a canonical retroflection type to an early retroflection highlighted in Figure 9. This also highlights how the presence of a high EKE in Figure 11a may be associated with the arrival of anticyclonic eddies as a cause of the early retroflection event but not its consequence.

A negative linear relationship with a correlation coefficient equal to 0.3, significant at 95% confidence, is found between the EMC speed and EKE in Figure 10 extracted from the canonical retroflection area illustrated as a blue box in Figure 11b. Figure 11e depicts the composite obtained for weaker EMC speeds (below one standard deviation) but with a more intense EKE (above one standard deviation) in Figure 11b. The retroflection type of the mean composite resulted in canonical retroflection. This reveals that the canonical retroflection pattern is associated with a decrease in EMC surface speeds and the generation of eddy dipoles after EMC separation on the leeward side of the southern tip of Madagascar (Ridderinkhof et al., 2013). Based on de Ruijter et al. (2004) and Ridderinkhof et al. (2013), eddy dipoles are typical patterns of the EMC southern extension, explaining the higher EKE seen when EMC is in a canonical retroflection mode.

The third pattern in Figure 11f is obtained from a mean composite of SSH associated with decreased EKE (below one standard deviation) in both early and canonical areas (blue and green boxes in Figures 11a and 11b). This corresponds to a no retroflection case. In this case, a straight flow toward the African continent is associated with a minimum in eddy activity in the early and canonical retroflection areas.

Figure 12 shows the capacity of retroflection areas to receive drifted anticyclonic eddies arriving from the central Indian Ocean. It shows trajectories of mesoscale anticyclonic eddies from the east into the

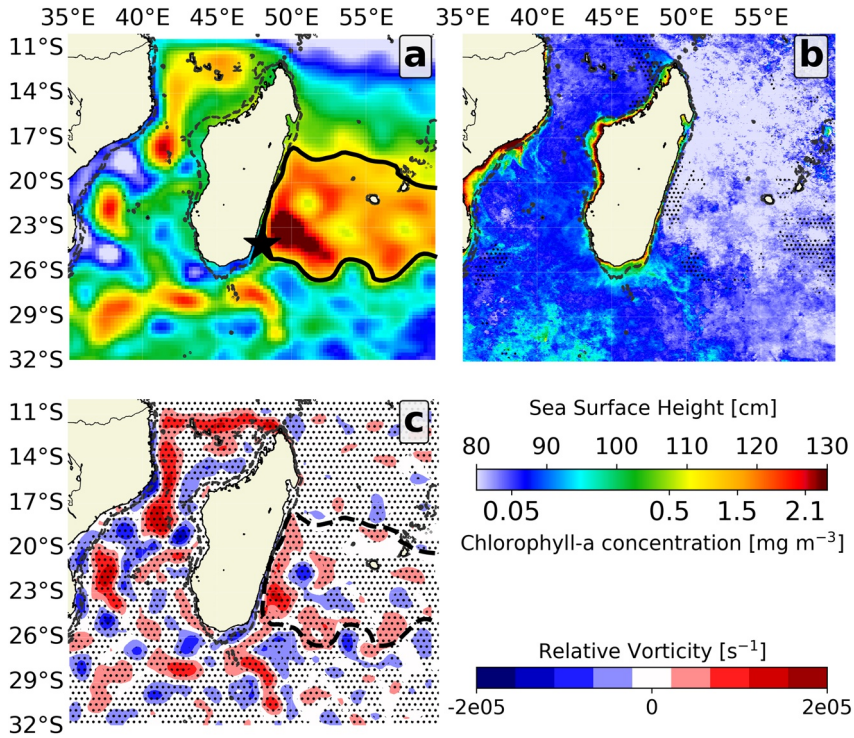

Figure 7. Spatial evidence of EMC early retroflection. (a) Composite of SSH for the periods of absolute EMC volume transport above the standard deviation (red plots in panel Figure 6a). The black contour and star indicate the identified mean EMC early retroflection extent. (b) Composites of chlorophyll-a concentration and (c) Relative vorticity for the same early retroflection periods. Hatched black dots indicate a 95% confidence level according to a two-tailed Student's *t*-test.

retroflection areas. Figure 12a shows the arrival of anticyclonic eddies ending into the early retroflection areas, while Figure 12b depicts anticyclonic eddy trajectories ending life in canonical retroflection areas. Their presence is consistent with the indicated locations for retroflections (green and blue stars in Figures 10d and 10e), which show the presence of remarkable EKE at each attributed retroflection location (blue and green boxes in Figures 10a and 10b). This is in line with the findings highlighted in Figures 8 and 9 regarding eddy activity involvement triggering retroflections. Hence, the presence of EMC retroflection is often associated with mesoscale eddies occurring in both the early retroflection and canonical retroflection areas. The eddy tracking method is limited to show the interaction between eddies and the mean flow. Although eddy tracking shows the presence and path of eddies, it is limited to revealing their interactions with the EMC if anticyclonic eddies are disintegrated or continue their paths after triggering retroflection. This is consequently not an appropriate approach to demonstrate eddy-mean flow interactions in this case. Laxenaire et al. (2020) explained the complex fate of eddies when satellite altimeters could no longer track mesoscale eddies during eddy tracking processes. Mesoscale eddies can take different forms after no longer being monitored by tracking eddy methods (Laxenaire et al., 2020). Hence, the eddy trajectories, through the eddy-tracking method, are insufficient to understand and explain the contribution of mesoscale eddy triggering retroflection.

To enlighten the dynamical interaction between eddy-mean flow leading instabilities of the EMC, the surface barotropic energy conversion rate is calculated to estimate the transfer of momentum between the mesoscale eddy and the mean flow (Figure 13). Since anticyclonic eddies contribute to the formation of retroflection, eddy activities in the retroflection areas will be mostly attributed to anticyclonic eddy dynamics. Figure 13 illustrates the surface barotropic energy conversion rate during the whole period of early and canonical retroflection combined (Figure 13a) and during the period of no retroflection (Figure 13b). Clear differences in transferred energy are found at southeast of Madagascar during these periods. The Mozambique channel side is also included intentionally in Figure 13 to show that other regions do not differ more

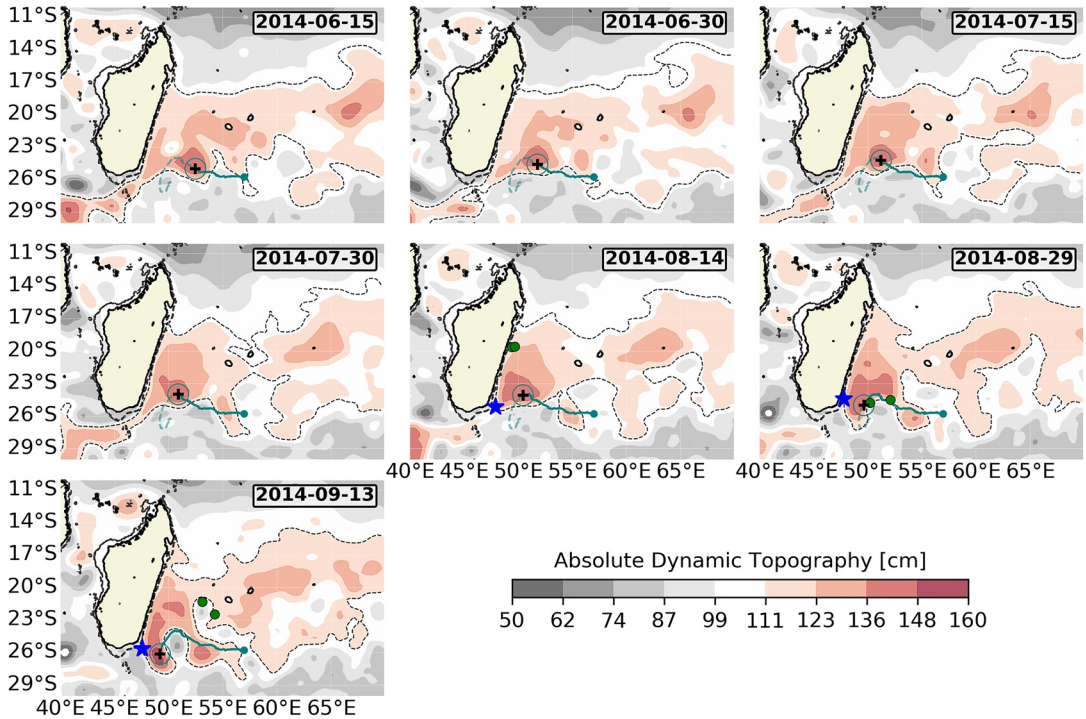

Figure 8. Synoptic development of EMC early retroflection from onset to full formation during the period of June 20 to September 13, 2014. Blue stars are the retroflection positioned, while the dotted black lines delineate the streamline of the flow. Maps in the background are the surface sea level at 15-day intervals from the period mentioned above. For all panels, the dark-cyan line represents the path of tracked anticyclonic eddies triggering early retroflection from the automated eddy-tracking product (Mason et al., 2014). The dot in dark cyan pins the location where the eddy was formed. The black cross surrounded by a circle denotes the progressive location of the tracked anticyclonic eddy. Green dots illustrate the released virtual particles to coincide with the full development of early retroflection. Virtual particles were released inside the EMC core, 50°E and 18°S, advected forward in time using velocity components derived from gridded altimetry products.

in terms of energy during the period of retroflections. The dipole of transferred energy is located southeast of the island (~25°S), in line with Halo et al. (2014) (see Figures 13a–13d). A negative value implies the transfer of energy from the mesoscale eddies to the mean flow, and a positive value implies the opposite. Figure 13a reveals a strong flow of kinetic energy on the order of 2.3 10^{-6} m^2 s^{-3} (negative value), is transferred from the eddy field to the EMC in the vicinity of 25°S. Figure 13b shows less transfer of momentum during the no retroflection event, indicated by only 0.8 10^{-6} m^2 s^{-3} (negative value). This reveals the interaction of anticyclonic eddies with the EMC in the early retroflection area. On the other hand, a flow of intense energy exceeding 2.3 10^{-6} m^2 $s—^{3}$ (positive value), is observed in the southern extension of the EMC (Figure 13a). This is due to the transfer of energy from the mean flow to the eddy. This reveals the capacity of the EMC southern extension propelling eddies, documented in de Ruijter et al. (2004), Ridderinkhof et al. (2013), and Halo et al. (2014), which trigger the condition toward formation of canonical retroflection at the southern tip explained in the previous paragraph. The case of less energy momentum in Figure 13b is characterized by less eddy activity and a stable EMC and, hence, no retroflection. The findings corroborate to the results in Figure 11, showing that high EKE in the retroflection areas promotes retroflection, while less EKE in both locations implies no retroflection. Hence, it is now demonstrated that high EKE located at the retroflection areas are indicative of eddy activities associated with the EMC to trigger retroflections.

In summary, the EMC early retroflection is linked with EMC strength. Anticyclonic eddies drifting from the central Indian Ocean to the east Madagascar coast favor early retroflection formation, anticyclonic eddies near the southern tip of Madagascar promote the generation of canonical retroflection, and no retroflection appears to be associated with a lower EKE, together with EMC strength modulation.

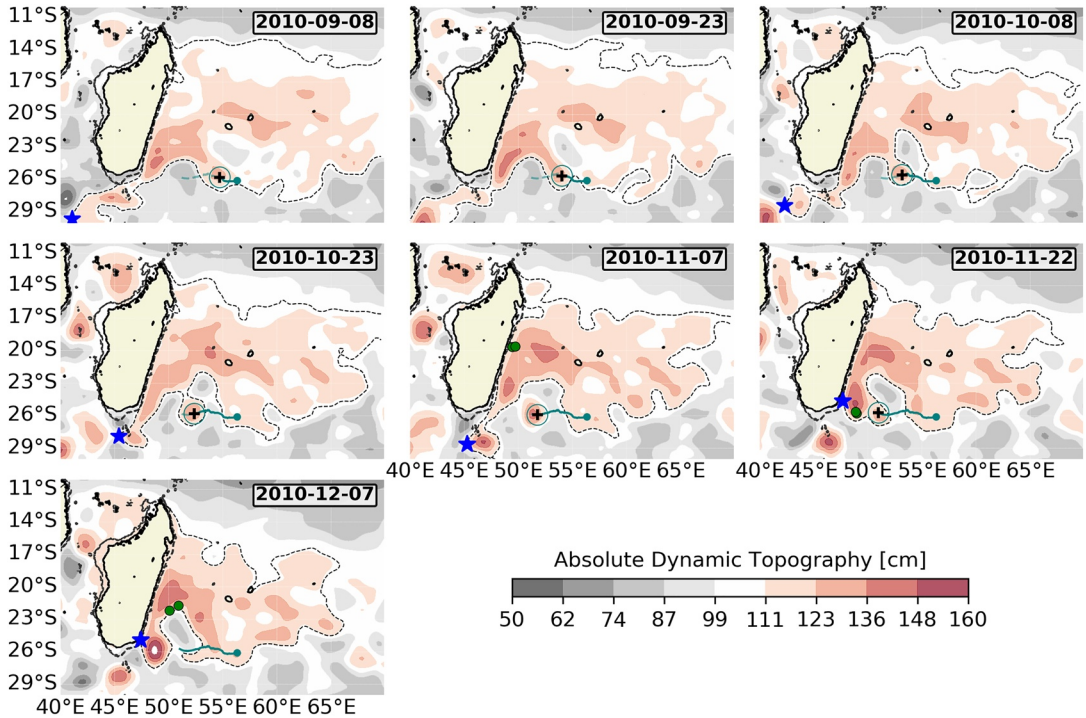

Figure 9. Synoptic development of EMC early retroflection from onset to full formation during the period of August 27 to December 7, 2010. Same description as in Figure 8.

3.5. Local and Regional Impact of the Early Retroflection

The retroflection structure allows an estimated lagged response with the south Madagascar coastal upwelling cell strength (Ramanantsoa et al., 2018) (Figure 14a). During an early retroflection, coastal upwelling became instantaneously weak (for one month), i.e., the upwelling cell surface temperature anomaly becomes warm, while EMC early retroflection occurs. The average composite of the SST anomaly during the period of the early retroflection event shows an abnormally high temperature in the upwelling cell (Figure 14b), while the period composite during the EMC canonical and no retroflection combined seems to be favorable for upwelling occurrences (Figure 14c). This behavior is probably due to the interruption of the topographically induced upwelling mechanical process (Ramanantsoa, 2018) that occurs during an early retroflection. The disruptions of the southward EMC flow, due to premature eastward veering causing the early detachment of the EMC from the coast, may inhibit the mechanism generating the upwelling strength of southeast Madagascar, so-called Core 1 (Ramanantsoa, 2018), which is the bottom Ekman transport

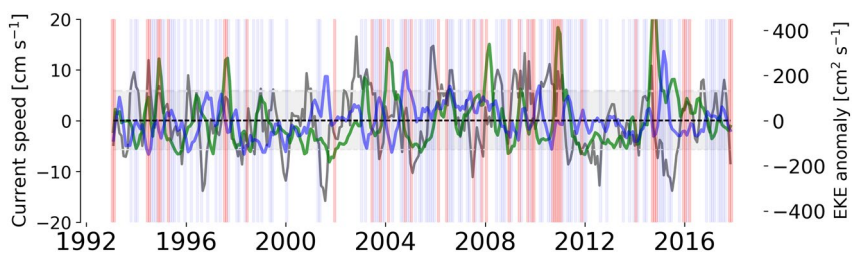

Figure 10. Dynamic processes associated with EMC retroflection cases. Gray time series is the monthly surface current speed anomalies of the EMC from the satellite altimetry. Time series was extracted at the same location of the moored ADCP used in Figure 5b. The gray shaded area delimits the time series standard deviation. The green (blue) time series presents the EKE extracted from the green (blue) box in Figures 11a and 11b. All signals are filtered using a three-month running mean. The red- and blue-colored bands indicate the EMC early retroflection and canonical retroflection events, respectively.

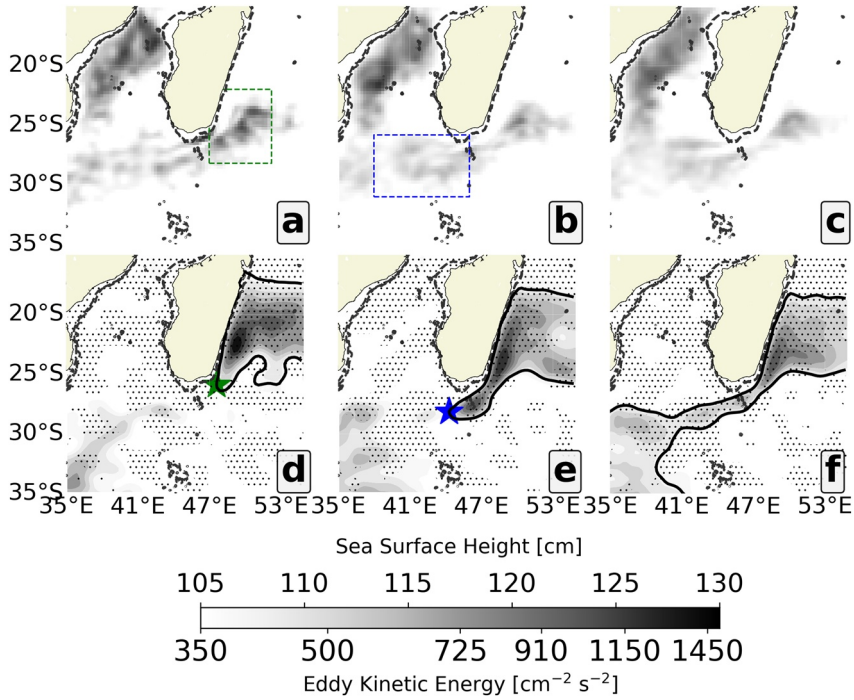

Figure 11. EMC velocity and EKE determining retroflection position. Panels (a)–(c) are composites of EKE occurring during each retroflection case. Panel (d) is the composite of the SSH when the EMC surface speeds and the EKE (green box in (a)) are abnormally higher, that is, above the first standard deviation. Panel (e) is the SSH composite corresponding to the period of weaker EMC surface speeds, below the standard deviation, but with a high EKE (blue box in (b)). Panel (f) is built from the composite of the period associated with weaker EKE for both green and blue boxes in panels (a) and (b). For panels (d) and (e), green and blue stars represent the EMC retroflection positions. Hatched black dots indicate a 95% confidence level according to a two-tailed Student's *t*-test.

inducing upwelling over the topography and reinforced by favorable winds at inter-annually time scale (Ramanantsoa et al., 2018).

A spatial coherent structure is found between composites of early retroflection circulation patterns and surface chlorophyll-a concentration during the same period (Figure 7b). Moreover, Figure 15 reveals that the prevalence of the austral summer South-East Madagascar bloom as described by Dilmahamod et al. (2019) could be mainly associated with an EMC early retroflection. Although this bloom generation is associated with multiple processes (Dilmahamod et al., 2019), the early retroflection could be a contributor to the summer bloom occurrence. In addition, the composite of surface currents built from early retroflection

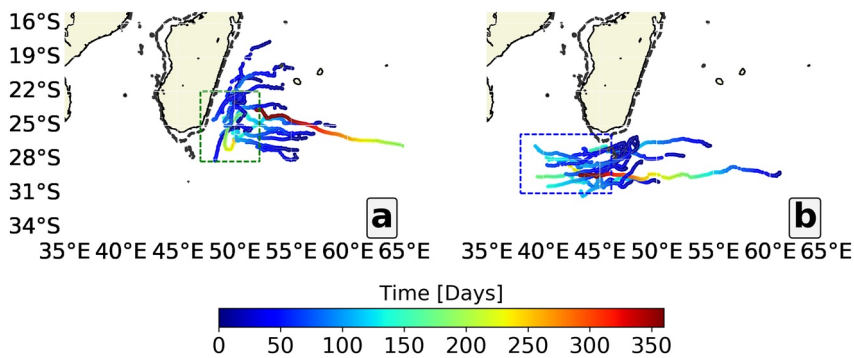

Figure 12. Anticyclonic eddies congregating in the retroflection areas. Panel (a) shows anticyclonic eddy trajectories drifting from the Indian Ocean into the green box defined in Figure 11a. Panel (b) also shows anticyclonic eddies that come from the east concentrating in the high EKE area identified in the blue box seen in Figure 11b.

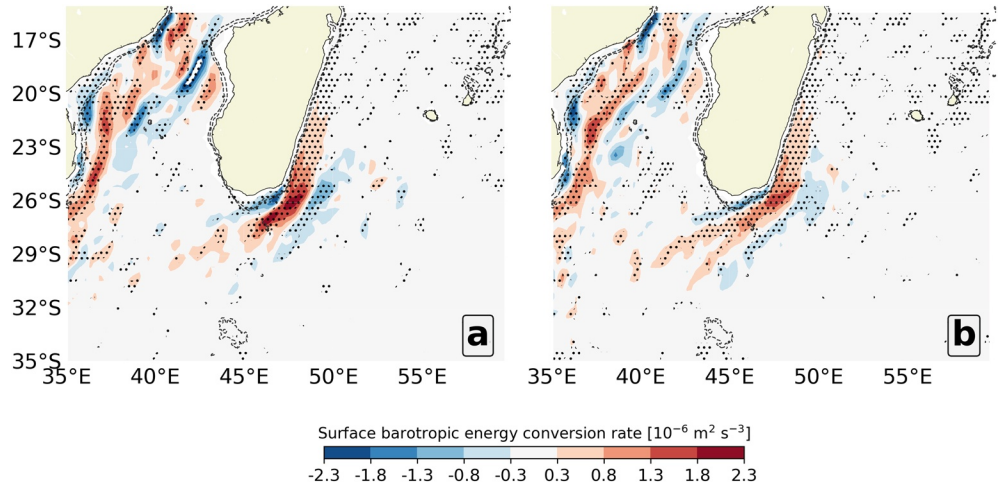

Figure 13. Transfer of kinetic energy between mesoscale eddies and the mean flow. Panel (a) presents the surface barotropic energy conversion rate during the period of both retroflections, early retroflection and canonical retroflection. Panel (b) surface barotropic energy conversion rate during the no retroflection period. A negative (positive) sign means that the direction of the transfer goes from the eddy field (mean flow) to the mean flow (eddy field) (Ma & Wang, 2014; Raj et al., 2016). Hatched black dots indicate a 95% confidence level according to a two-tailed Student's *t*-test.

periods (Figure 15a) reveals that the EMC early retroflection structure could act as a contributor to SICC formation (Menezes et al., 2016). This suggests that the transport of nutrient-rich water through the SICC from the east coast could induce a visible offshore chlorophyll-a concentration patch (Figures 7b and 15b). Moreover, virtual particle simulations during the synoptic development of early retroflection in Figures 8 and 9 reinforce the concept of offshore nutrient advection from the east coast of Madagascar drifting toward the SICC. This finding agrees with Srokosz et al. (2015) and Dilmahamod et al. (2019), who associated early retroflection as a factor triggering the prominence of phytoplankton blooms.

Hence, the occurrence of EMC Early Retroflection has a contrasting effect: While it perturbs the functioning of coastal upwelling south of Madagascar, it also tends to favor the South-East Madagascar bloom. Both are important for biology and fisheries.

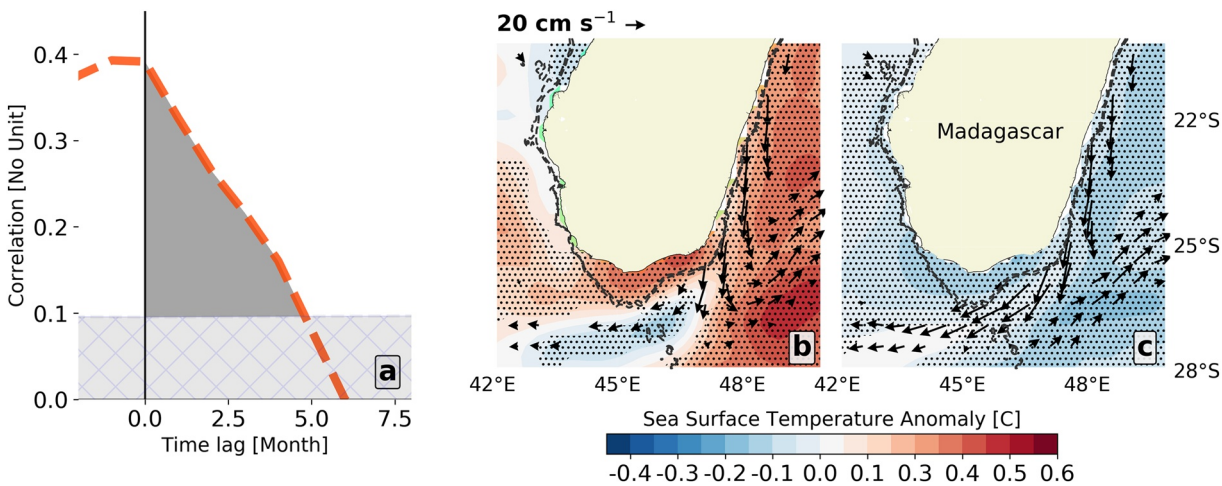

Figure 14. Impact of the EMC retroflection on coastal upwelling. (a) Lag correlation between the longitudinal EMC retroflection positions and the coastal upwelling surface temperature anomalies (Ramanantsoa et al., 2018). Panel (b) shows a composite period of the SST anomaly during early retroflection events. Arrows depict surface geostrophic currents and stating the early retroflection flow. Similarly, Panel (c) represents a composite period of the SST anomaly during canonical and no retroflection events. Circles in (b red) and (c blue) emphasize the SST anomalies in the upwelling cell area. For both panels (b) and (c), only surface currents above 10 cm s^{-1} are shown. Hatched black dots indicate a 95% confidence level according to a two-tailed Student's *t*-test.

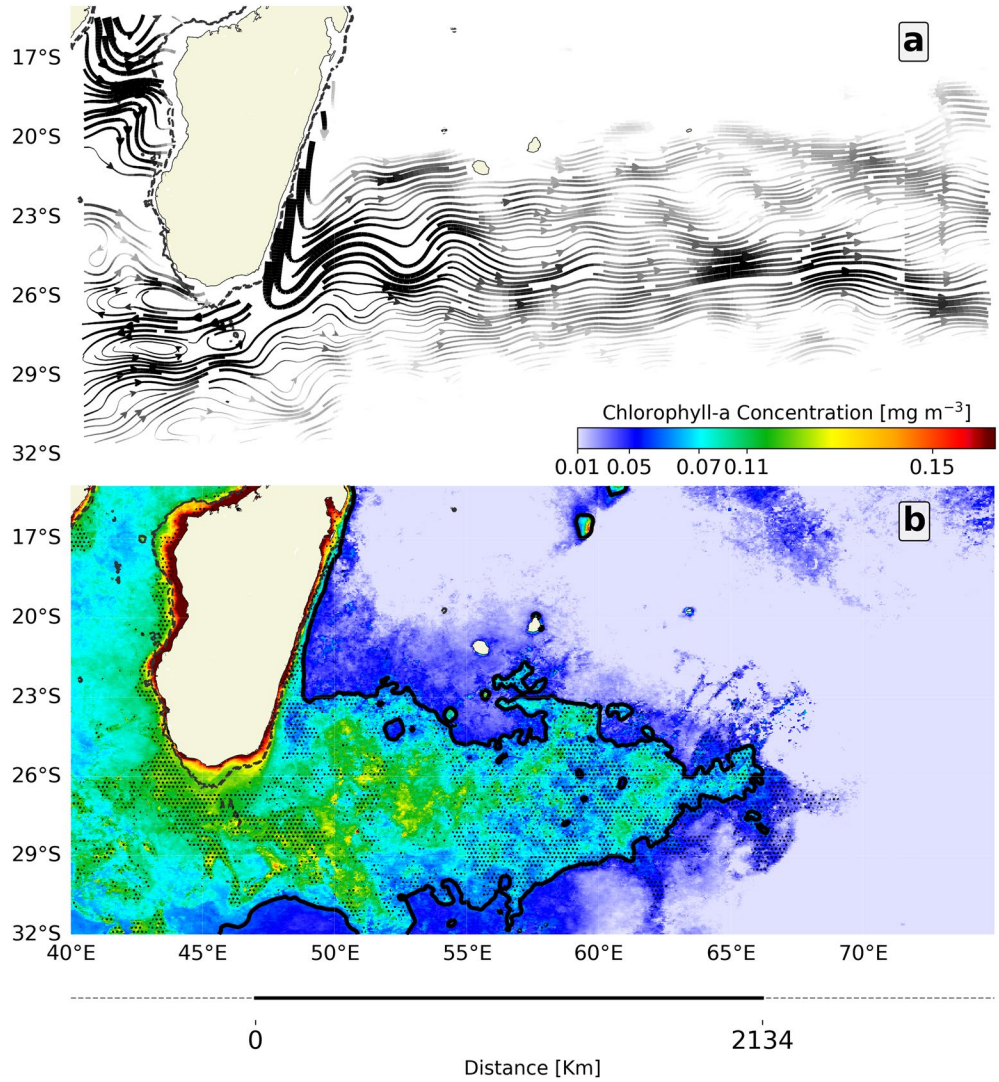

Figure 15. Connection between the EMC retroflection and the southeast Madagascar phytoplankton bloom. (a) Composite period of surface current directions during the EMC early retroflection periods. Only current speeds above 10 cm s^{-1} are shown. (b) Composite period of chlorophyll-*a* concentration during the periods of EMC early retroflection occurrences in austral summer. Contour depicts the 0.07 mg m^{-3} chlorophyll-*a* concentration in line with Dilmahamod et al. (2019). Hatched black dots indicate a 95% confidence level according to a two-tailed Student's t-test in (b), while confidence level for (a) has been done in previous figures and it is not reproduced to preserve its esthetic.

The disruptions of anticyclonic eddy pulses due to early retroflection and canonical retroflection should be assessed if they induce sensitivity in the Agulhas Current System activities since mesoscale structures originating south of Madagascar are a major source of Agulhas Current water (de Ruijter et al., 2004; Penven, Lutjeharms, et al., 2006). A separate study should investigate the cascade effect of EMC retroflection on Agulhas Current retroflection positioning if the Agulhas Current System remains stable due to this disruption of energy transferred through eddies from EMC.

4. Discussion and Conclusions

Using a suite of cruise data measurements, in situ data, and satellite observations, this study reveals the spatial extent of the EMC retroflection. Three distinct types of states are identified: early retroflection, canonical retroflection, and no retroflection. The classic retroflection south of Madagascar, beyond the southern tip, is here defined as a canonical retroflection. The new state, the EMC early retroflection, corresponds to

the current turning back offshore from the east coast of the island. A retroflection position detected close to the African coastline until further downstream in the Agulhas Current System is described as no retroflection. From 1993 to 2017, retroflections occurred 47% of the time, 13% of which were attributed to the early retroflection. These findings corroborate the results highlighted by Siedler et al. (2009), who revealed that almost 50% of the EMC water feeds the Agulhas Current System, while ~40% contributes to SICC formation.

By linking EMC strength and the mesoscale variability occurring in the retroflection areas, our study also shows how retroflection can be formed. The retroflection position is EMC strength dependent, that is, anomalous EMC speed favor retroflection, with a significant eddy activity contribution. Synoptic development of early retroflection demonstrated the progressive formation of the premature eastward drift of the EMC core at 25°S after interacting with an anticyclonic eddy (Figures 8 and 9). The availability of long-term observations of the EMC strength allowed us to conclude that the variability of EMC volume transport (column water) varies with the occurrence numbers of early retroflection (Figure 6). The surface signature of this early retroflection was subsequently observed and confirmed by multisensor satellite products, altimeters and ocean colors (Figure 7). Hence, an intense current can promote early retroflection occurrences in agreement with processes described in Ou and De Ruijter (1986) during investigation of the Agulhas Current retroflection mode, as a western boundary current having similar characteristics as the EMC.

The retroflection type is defined by the variation in the EKE in the retroflection areas, early retroflection and canonical retroflection areas and is associated with EMC strength modulation. Anomalously high EKE in these areas was demonstrated to trigger the formation of retroflection. Weaker EKEs in both the early retroflection (east) and canonical retroflection areas (west) promote the no retroflection case with a continuous flow propagating from the EMC southern extension straight towards the Agulhas Current without interruption (Figure 11). The findings respond to the question of how the mesoscale eddy interacts with the EMC. Transfer of a strong EKE from the mesoscale eddy field to the EMC is found during the retroflection periods, while less transfer of momentum is implied during the no retroflection period (Figure 12). Similar events of eddy-current interactions have been described upstream of the Agulhas Current, where entrainment of anticyclonic eddies increases the current velocity and shifts the Agulhas Current offshore (Braby et al., 2016). Additionally, the positive transfer of momentum (Figure 13a), from the mean flow to the eddy field, favors the presence of an anticyclonic standing eddy at the southern tip of Madagascar propelled by the EMC before the formation of eddy dipoles (de Ruijter et al., 2004; Ridderinkhof et al., 2013), which promotes the canonical retroflection case.

The irregular arrival of Rossby waves and impinged eddies, originating from the Indian Ocean and congregating at 25°S (de Ruijter et al., 2004; Halo et al., 2014; Quartly et al., 2006; Schouten et al., 2002, 2003), induced difficulties in clearly identifying the original location of the EMC retroflection and the source of the SICC from VMADCP observations (Figure 2). The combination of altimetry within situ data reveals that anticyclonic eddies passing through 25°S are associated with retroflection in addition to the contribution of the EMC core strength. Since it was difficult to interpret the early retroflection as a retroflection in previous literature (Lutjeharms, 1988; Quartly & Srokosz, 2002), this study has devoted significant effort to showing the evidence, as well as to describing the dynamic processes and the impact of the early EMC eastward veering from the coast at 25°S.

Identification of the EMC retroflection patterns leads to an understanding of their influence on the southeastern Madagascar Bloom, coastal upwelling, and connection with the SICC. Early retroflection has several effects on local ecosystems. It favors a prevailing southeast phytoplankton bloom (Figure 14) but disrupts the prominence of coastal upwelling, as seen in Figures 13a and 13b. According to Backeberg et al. (2012) (see their Figure 4), mesoscale variability of the southwest Indian Ocean, including south of Madagascar, has intensified due to the enhancement of trade winds over the tropical region. This may increase EMC early retroflection in numbers due to the increase in mesoscale eddy activity, and consequently, it may induce more southeastern Madagascar Bloom but weaken coastal upwelling.

More in situ data sets, such as long-term observations and ARGO data, are required for a better understanding of the physical mechanisms associated with western boundary currents interacting with mesoscale eddies (anticyclonic and/or cyclonic). Moreover, the effect of the EMC retroflection mode on the Agulhas Current and the Indian Ocean gyre should be assessed in a separate study.

Data Availability Statement

Data sets are available through the ZKO data portal (http://data.zkonet.nl/). The authors thank Prof Martin Visbeck (GEOMAR) and Dr Raymond Roman (UCT) for providing some cruise data sets utilized in this study. Ocean dynamic topography data were obtained from the Copernicus Marine Environment Monitoring Service (CMEMS) (http://marine.copernicus.eu/). The global drifter data used in this study were collected from the National Oceanic and Atmospheric Administration (NOAA), Physical Oceanography Division (PhOD), and Global Drifter Program (https://www.aoml.noaa.gov/phod/gdp/).

Acknowledgments
The authors want to thank the NRF SARCHi chair on Ocean Atmosphere Modeling, the GdRI-Sud CROCO project, and the Nansen program for funding. The volume transport data were sampled within the context of the INATEX program funded by, Netherlands Organization for Scientific Research (NWO), section Earth and Life Sciences (ALW) through its ZKO Grant 839.08.431. The altimeter Mesoscale Eddy Trajectory Atlas products were produced by SSALTO/DUACS and distributed by AVISO+ (https://www.aviso.altimetry.fr/) with support from CNES, in collaboration with Oregon State University with support from NASA.

References

AbdAllah, L., & Shimshoni, I. (2016). K-means over incomplete datasets using mean Euclidean distance. In *International conference on machine learning and data mining in pattern recognition* (pp. 113–127). https://doi.org/10.1007/978-3-319-41920-6_9

Anggoro, S. (2017). The dynamics of sea surface height and geostrophic current in the Arafura Sea. In *IOP Conference Series: Earth and Environmental Science* (Vol. *55*, p. 012046). IOP Publishing.

Arruda, W., Zharkov, V., Deremble, B., Nof, D., & Chassignet, E. (2014). A new model of current retroflection applied to the westward protrusion of the Agulhas current. *Journal of Physical Oceanography*, *44*(12), 3118–3138. https://doi.org/10.1175/jpo-d-14-0054.1

Backeberg, B. C., Penven, P., & Rouault, M. (2012). Impact of intensified Indian Ocean winds on mesoscale variability in the Agulhas system. *Nature Climate Change*, *2*(8), 608–612. https://doi.org/10.1038/nclimate1587

Beal, L. M., De Ruijter, W. P., Biastoch, A., Zahn, R., & Zahn, R. (2011). On the role of the Agulhas system in ocean circulation and climate. *Nature*, *472*(7344), 429–436. https://doi.org/10.1038/nature09983

Bemiasa, J. (2009). *Dynamique des pecheries traditionnelles d'anchois, de calmars et de poulpes du sud-ouest de Madagascar: Utilisation d'outils oceanographiques pour la gestion des ressources. (Doctoral dissertation)*. Universite de Toliara, Madagascar. Retrieved from http://archimer.ifremer.fr/doc/2009/these-6847.pdf

Braby, L., Backeberg, B. C., Ansorge, I., Roberts, M. J., Krug, M., & Reason, C. J. (2016). Observed eddy dissipation in the Agulhas Current. *Geophysical Research Letters*, *43*(15), 8143–8150. https://doi.org/10.1002/2016GL069480

Cancet, M., Griffin, D., Cahill, M., Chapron, B., Johannessen, J., & Donlon, C. (2019). Evaluation of globcurrent surface ocean current products: A case study in Australia. *Remote Sensing of Environment*, *220*, 71–93. https://doi.org/10.1016/j.rse.2018.10.029

Chapman, P., Di Marco, S., Davis, R., & Coward, A. (2003). Flow at intermediate depths around Madagascar based on ALACE float trajectories. *Deep Sea Research Part II: Topical Studies in Oceanography*, *50*(12–13), 1957–1986. https://doi.org/10.1016/s0967-0645(03)00040-7

Chassignet, E. P., Hurlburt, H. E., Smedstad, O. M., Halliwell, G. R., Hogan, P. J., Wallcraft, A. J., & Bleck, R. (2007). The HYCOM (hybrid coordinate ocean model) data assimilative system. *Journal of Marine Systems*, *65*(1–4), 60–83. https://doi.org/10.1016/j.jmarsys.2005.09.016

Chelton, D. B., Schlax, M. G., & Samelson, R. M. (2011). Global observations of nonlinear mesoscale eddies. *Progress in Oceanography*, *91*(2), 167–216. https://doi.org/10.1016/j.pocean.2011.01.002

Chen, Z., Wu, L., Qiu, B., Sun, S., & Jia, F. (2014). Seasonal variation of the south equatorial current bifurcation off Madagascar. *Journal of Physical Oceanography*, *44*(2), 618–631. https://doi.org/10.1175/jpo-d-13-0147.1

de Ruijter, W. P., van Aken, H. M., Beier, E. J., Lutjeharms, J. R., Matano, R. P., & Schouten, M. W. (2004). Eddies and dipoles around South Madagascar: Formation, pathways and large-scale impact. *Deep Sea Research Part I: Oceanographic Research Papers*, *51*(3), 383–400. https://doi.org/10.1016/j.dsr.2003.10.011

Delepoulle, A., Chelton, D., Schlax, M., Faugere, Y., & Dibarboure, G. (2018). 24 year mesoscale eddy trajectory atlas on AVISO. In *EGU General Assembly Conference Abstracts* (Vol. 20, p. 13690). https://doi.org/10.1029/2018JC014582

Deo, A., Ganer, D., & Nair, G. (2011). Tropical cyclone activity in global warming scenario. *Natural Hazards*, *59*(2), 771–786. https://doi.org/10.1007/s11069-011-9794-8

Dilmahamod, A. F., Aguiar-González, B., Penven, P., Reason, C., De Ruijter, W., Malan, N., & Hermes, J. (2018). SIDDIES corridor: A major east-west pathway of long-lived surface and subsurface eddies crossing the subtropical South Indian Ocean. *Journal of Geophysical Research: Oceans*, *123*(8), 5406–5425. https://doi.org/10.1029/2018jc013828

Dilmahamod, A. F., Penven, P., Aguiar-González, B., Reason, C., & Hermes, J. (2019). A new definition of the South-East Madagascar bloom and analysis of its variability. *Journal of Geophysical Research: Oceans*, *124*(3), 1717–1735. https://doi.org/10.1029/2018JC014582

Ducet, N., Le Traon, P.-Y., & Reverdin, G. (2000). Global high-resolution mapping of ocean circulation from TOPEX/Poseidon and ERS-1 and -2. *Journal of Geophysical Research: Oceans*, *105*(C8), 19477–19498. https://doi.org/10.1029/2000jc900063

Feng, M., Weller, E., & Hill, K. (2009). The Leeuwin current. In E. S. Poloczanska, A. J. Hobday, & A. J. Richardson (Eds.), *A marine climate change impacts and adaptation report card for Australia 2009*. NCCARF Publication.

Feng, M., Zhang, N., Liu, Q., & Wijffels, S. (2018). The Indonesian Throughflow, its variability and centennial change. *Geoscience Letters*, *5*(1), 1–10. https://doi.org/10.1186/s40562-018-0102-2

Gordon, A. L., Ma, S., Olson, D. B., Hacker, P., Ffield, A., Talley, L. D., et al. (1997). Advection and diffusion of Indonesian Throughflow water within the Indian Ocean south equatorial current. *Geophysical Research Letters*, *24*(21), 2573–2576. https://doi.org/10.1029/97gl01061

Gwilliam, C., Coward, A., De Cuevas, B., Webb, D., Rourke, E., Thompson, S., & Döös, K. (1997). The OCCAM global ocean model. In *Proceedings of the second unam-cray supercomputing conference: Numerical simulations in the environmental and earth sciences* (pp. 24–30).

Halo, I., Backeberg, B., Penven, P., Ansorge, I., Reason, C., & Ullgren, J. (2014). Eddy properties in the Mozambique Channel: A comparison between observations and two numerical ocean circulation models. *Deep Sea Research Part II: Topical Studies in Oceanography*, *100*, 38–53. https://doi.org/10.1016/j.dsr2.2013.10.015

Hartigan, J. A., & Wong, M. A. (1979). Ak-means clustering algorithm. *Journal of the Royal Statistical Society: Series C (Applied Statistics)*, *28*(1), 100–108. https://doi.org/10.2307/2346830

Hastenrath, S. (2000). Zonal circulations over the equatorial Indian Ocean. *Journal of Climate*, *13*(15), 2746–2756. https://doi.org/10.1175/1520-0442(2000)013<2746:zcotei>2.0.co;2

Ho, C.-R., Zheng, Q., & Kuo, N.-J. (2004). Seawifs observations of upwelling south of Madagascar: Long-term variability and interaction with East Madagascar current. *Deep Sea Research Part II: Topical Studies in Oceanography*, *51*(1–3), 59–67. https://doi.org/10.1016/j.dsr2.2003.05.001

Hu, S., & Fedorov, A. V. (2019). Indian Ocean warming can strengthen the Atlantic meridional overturning circulation. *Nature Climate Change*, *9*(10), 747–751. https://doi.org/10.1038/s41558-019-0566-x

Jia, F., Wu, L., Lan, J., & Qiu, B. (2011). Interannual modulation of eddy kinetic energy in the southeast Indian Ocean by southern annular mode. *Journal of Geophysical Research: Oceans*, *116*(C2). https://doi.org/10.1029/2010jc006699

Johannessen, J., Chapron, B., Collard, F., Rio, M., Piollé, J., Gaultier, L., et al. (2016). *Globcurrent: Multisensor synergy for surface current estimation*.

Jose, Y. S., Penven, P., Aumont, O., Machu, E., Moloney, C., Shillington, F., & Maury, O. (2016). Suppressing and enhancing effects of mesoscale dynamics on biological production in the Mozambique channel. *Journal of Marine Systems*, *158*, 129–139. https://doi.org/10.1016/j.jmarsys.2016.02.003

Lambert, E., Bars, D. L., & de Ruijter, W. P. (2016). The connection of the Indonesian Throughflow, south Indian Ocean countercurrent and the Leeuwin current. *Ocean Science*, *12*(3), 771–780. https://doi.org/10.5194/os-12-771-2016

Laxenaire, R., Speich, S., & Stegner, A. (2020). Agulhas ring heat content and transport in the south Atlantic estimated by combining satellite altimetry and Argo profiling floats data. *Journal of Geophysical Research: Oceans*, *125*(9), e2019JC015511. https://doi.org/10.1029/2019jc015511

Liu, Y., Weisberg, R. H., Vignudelli, S., & Mitchum, G. T. (2014). Evaluation of altimetry-derived surface current products using Lagrangian drifter trajectories in the eastern Gulf of Mexico. *Journal of Geophysical Research: Oceans*, *119*(5), 2827–2842. https://doi.org/10.1002/2013jc009710

Longhurst, A. (2001). A major seasonal phytoplankton bloom in the Madagascar basin. *Deep Sea Research Part I: Oceanographic Research Papers*, *48*(11), 2413–2422. https://doi.org/10.1016/S0967-0637(01)00024-3

Loveday, B. R., Durgadoo, J. V., Reason, C. J., Biastoch, A., & Penven, P. (2014). Decoupling of the Agulhas leakage from the Agulhas Current. *Journal of Physical Oceanography*, *44*(7), 1776–1797. https://doi.org/10.1175/jpo-d-13-093.1

Lumpkin, R., Maximenko, N., & Pazos, M. (2012). Evaluating where and why drifters die. *Journal of Atmospheric and Oceanic Technology*, *29*(2), 300–308. https://doi.org/10.1175/jtech-d-11-00100.1

Lumpkin, R., & Pazos, M. (2007). Measuring surface currents with surface velocity program drifters: The instrument, its data, and some recent results. *Lagrangian Analysis and Prediction of Coastal and Ocean Dynamics*, 39–67.

Lutjeharms, J. (1976). The Agulhas current system during the northeast monsoon season. *Journal of Physical Oceanography*, *6*(5), 665–670. https://doi.org/10.1175/1520-0485(1976)006<0665:tacsdt>2.0.co;2

Lutjeharms, J. (1988). Remote sensing corroboration of retroflection of the east Madagascar current. *Deep Sea Research Part A. Oceanographic Research Papers*, *35*(12), 2045–2050. https://doi.org/10.1016/0198-0149(88)90124-0

Lutjeharms, J. (2006). *The Agulhas Current* (Vol. *329*). Springer.

Lutjeharms, J., Bang, N., & Duncan, C. (1981). Characteristics of the currents east and south of Madagascar. *Deep Sea Research Part A. Oceanographic Research Papers*, *28*(9), 879–899. https://doi.org/10.1016/0198-0149(81)90008-X

Lutjeharms, J., & Van Ballegooyen, R. (1988). The retroflection of the Agulhas current. *Journal of Physical Oceanography*, *18*(11), 1570–1583. https://doi.org/10.1175/1520-0485(1988)018<1570:trotac>2.0.co;2

Ma, L., & Wang, Q. (2014). Interannual variations in energy conversion and interaction between the mesoscale eddy field and mean flow in the Kuroshio south of Japan. *Chinese Journal of Oceanology and Limnology*, *32*(1), 210–222. https://doi.org/10.1007/s00343-014-3036-3

Mason, E., Pascual, A., & McWilliams, J. C. (2014). A new sea surface height-based code for oceanic mesoscale eddy tracking. *Journal of Atmospheric and Oceanic Technology*, *31*(5), 1181–1188. https://doi.org/10.1175/JTECH-D-14-00019.1

Maximenko, N., Hafner, J., & Niiler, P. (2012). Pathways of marine debris derived from trajectories of Lagrangian drifters. *Marine Pollution Bulletin*, *65*(1–3), 51–62. https://doi.org/10.1016/j.marpolbul.2011.04.016

Menezes, V. V., Phillips, H. E., Schiller, A., Bindoff, N. L., Domingues, C. M., & Vianna, M. L. (2014). South Indian countercurrent and associated fronts. *Journal of Geophysical Research: Oceans*, *119*(10), 6763–6791. https://doi.org/10.1002/2014jc010076

Menezes, V. V., Phillips, H. E., Vianna, M. L., & Bindoff, N. L. (2016). Interannual variability of the south Indian countercurrent. *Journal of Geophysical Research: Oceans*, *121*(5), 3465–3487. https://doi.org/10.1002/2015jc011417

Menezes, V. V., & Vianna, M. L. (2019). Quasi-biennial Rossby and Kelvin waves in the south Indian Ocean: Tropical and subtropical modes and the Indian Ocean dipole. *Deep Sea Research Part II: Topical Studies in Oceanography*, *166*, 43–63. https://doi.org/10.1016/j.dsr2.2019.05.002

Nauw, J., Van Aken, H., Lutjeharms, J., & De Ruijter, W. (2006). Intrathermocline eddies in the southern Indian Ocean. *Journal of Geophysical Research: Oceans*, *111*(C3). https://doi.org/10.1029/2005JC002917

Nauw, J., Van Aken, H., Webb, A., Lutjeharms, J., & De Ruijter, W. (2008). Observations of the southern East Madagascar Current and undercurrent and countercurrent system. *Journal of Geophysical Research: Oceans*, *113*(C8). https://doi.org/10.1029/2007JC004639

Niiler, P. (2001). The world ocean surface circulation. In *International Geophysics* (Vol. 77, pp. 193–204). Elsevier. https://doi.org/10.1016/s0074-6142(01)80119-4

Olson, D. B., & Evans, R. H. (1986). Rings of the Agulhas current. *Deep Sea Research Part A. Oceanographic Research Papers*, *33*(1), 27–42. https://doi.org/10.1016/0198-0149(86)90106-8

Ou, H. W., & De Ruijter, W. P. (1986). Separation of an inertial boundary current from a curved coastline. *Journal of Physical Oceanography*, *16*(2), 280–289. https://doi.org/10.1175/1520-0485(1986)016<0280:SOAIBC>2.0.CO;2

Palastanga, V., Van Leeuwen, P., & De Ruijter, W. (2006). A link between low-frequency mesoscale eddy variability around Madagascar and the large-scale Indian Ocean variability. *Journal of Geophysical Research: Oceans*, *111*(C9). https://doi.org/10.1029/2005jc003081

Palastanga, V., Van Leeuwen, P., Schouten, M., & De Ruijter, W. (2007). Flow structure and variability in the subtropical Indian Ocean: Instability of the south Indian Ocean Countercurrent. *Journal of Geophysical Research: Oceans*, *112*(C1). https://doi.org/10.1029/2005jc003395

Penven, P., Debreu, L., Marchesiello, P., & McWilliams, J. C. (2006). Evaluation and application of the ROMS 1-way embedding procedure to the central California upwelling system. *Ocean Modelling*, *12*(1–2), 157–187. https://doi.org/10.1016/j.ocemod.2005.05.002

Penven, P., Lutjeharms, J., & Florenchie, P. (2006). Madagascar: A pacemaker for the Agulhas Current system? *Geophysical Research Letters*, *33*(17). https://doi.org/10.1029/2006GL026854

Ponsoni, L., Aguiar-González, B., Maas, L., van Aken, H., & Ridderinkhof, H. (2015). Long-term observations of the east Madagascar undercurrent. *Deep Sea Research Part I: Oceanographic Research Papers*, *100*, 64–78. https://doi.org/10.1016/j.dsr.2015.02.004

Ponsoni, L., Aguiar-Gonzalez, B., Nauw, J. J., Janine, H., Ridderinkhof, L. R. M., & Maas, L. R. (2015). First observational evidence of a north Madagascar undercurrent. *Dynamics of Atmospheres and Oceans*, *72*, 12–20. https://doi.org/10.1016/j.dynatmoce.2015.08.002

Ponsoni, L., Aguiar-González, B., Ridderinkhof, H., & Maas, L. R. (2016). The east Madagascar current: Volume transport and variability based on long-term observations. *Journal of Physical Oceanography*, *46*(4), 1045–1065. https://doi.org/10.1175/jpo-d-15-0154.1

Quartly, G. D., Buck, J. J., Srokosz, M. A., & Coward, A. C. (2006). Eddies around Madagascar—The retroflection re-considered. *Journal of Marine Systems*, *63*(3), 115–129. https://doi.org/10.1016/j.jmarsys.2006.06.001

Quartly, G. D., & Srokosz, M. A. (2002). Satellite observations of the Agulhas Current system. *Philosophical Transactions of the Royal Society of London, Series A: Mathematical, Physical and Engineering Sciences*, *361*, 51–56. https://doi.org/10.1098/rsta.2002.1107

Raj, R., Johannessen, J., Eldevik, T., Nilsen, J. Ø., & Halo, I. (2016). Quantifying mesoscale eddies in the Lofoten basin. *Journal of Geophysical Research: Oceans*, *121*(7), 4503–4521. https://doi.org/10.1002/2016jc011637

Raj, R. P., Peter, B. N., & Pushpadas, D. (2010). Oceanic and atmospheric influences on the variability of phytoplankton bloom in the southwestern Indian Ocean. *Journal of Marine Systems*, *82*(4), 217–229. https://doi.org/10.1016/j.jmarsys.2010.05.009

Ramanantsoa, J. D., Krug, M., Penven, P., Rouault, M., & Gula, J. (2018). Coastal upwelling south of Madagascar: Temporal and spatial variability. *Journal of Marine Systems*, *178*, 29–37. https://doi.org/10.1016/j.jmarsys.2017.10.005

Ramanantsoa, J. D., Penven, P., Krug, M., Rouault, M., Gula, J. (2018). Uncovering a new current: The southwest Madagascar coastal current. *Geophysical Research Letters*, *45*(4), 1930–1938. https://doi.org/10.1002/2017gl075900

Ramanantsoa, J. D. (2018). *Variability of coastal upwelling south of Madagascar (Doctoral dissertation)*. University of Cape Town. Retrieved from https://open.uct.ac.za/handle/11427/29859

Rao, S. A., Dhakate, A. R., Saha, S. K., Mahapatra, S., Chaudhari, H. S., Pokhrel, S., & Sahu, S. K. (2012). Why is Indian Ocean warming consistently? *Climatic Change*, *110*(3), 709–719. https://doi.org/10.1007/s10584-011-0121-x

Renault, L., McWilliams, J. C., & Penven, P. (2017). Modulation of the Agulhas Current retroflection and leakage by oceanic current interaction with the atmosphere in coupled simulations. *Journal of Physical Oceanography*, *47*(8), 2077–2100. https://doi.org/10.1175/JPO-D-16-0168.1

Reynolds, R. W., Smith, T. M., Liu, C., Chelton, D. B., Casey, K. S., & Schlax, M. G. (2007). Daily high-resolution-blended analyses for sea surface temperature. *Journal of Climate*, *20*(22), 5473–5496. https://doi.org/10.1175/2007jcli1824.1

Ridderinkhof, W., Le Bars, D., Von der Heydt, A., & De Ruijter, W. (2013). Dipoles of the south east Madagascar current. *Geophysical Research Letters*, *40*(3), 558–562. https://doi.org/10.1002/grl.50157

Rio, M.-H., & Santoleri, R. (2018). Improved global surface currents from the merging of altimetry and sea surface temperature data. *Remote sensing of Environment*, *216*, 770–785. https://doi.org/10.1016/j.rse.2018.06.003

Saji, N., Goswami, B., Vinayachandran, P., & Yamagata, T. (1999). A dipole mode in the tropical Indian Ocean. *Nature*, *401*(6751), 360–363. https://doi.org/10.1038/43854

Saunders, P. M., Coward, A. C., & de Cuevas, B. A. (1999). Circulation of the Pacific Ocean seen in a global ocean model: Ocean circulation and climate advanced modelling project (OCCAM). *Journal of Geophysical Research: Oceans*, *104*(C8), 18281–18299. https://doi.org/10.1029/1999jc900091

Schlax, M. G., & Chelton, D. B. (2016). *The "growing method" of eddy identification and tracking in two and three dimensions* (Vol. *8*). College of Earth, Ocean and Atmospheric Sciences, Oregon State University.

Schott, F. A., Xie, S.-P., & McCreary, J. P., Jr. (2009). Indian Ocean circulation and climate variability. *Reviews of Geophysics*, *47*(1). https://doi.org/10.1029/2007rg000245

Schouten, M. W., De Ruijter, W. P., & Van Leeuwen, P. J. (2002). Upstream control of Agulhas ring shedding. *Journal of Geophysical Research: Oceans*, *107*(C8), 23–31. https://doi.org/10.1029/2001jc000804

Schouten, M. W., de Ruijter, W. P., Van Leeuwen, P. J., & Ridderinkhof, H. (2003). Eddies and variability in the Mozambique Channel. *Deep Sea Research Part II: Topical Studies in Oceanography*, *50*(12–13), 1987–2003. https://doi.org/10.1016/S0967-0645(03)00042-0

Sheppard, C. R. (2003). Predicted recurrences of mass coral mortality in the Indian Ocean. *Nature*, *425*(6955), 294–297. https://doi.org/10.1038/nature01987

Siedler, G., Rouault, M., Biastoch, A., Backeberg, B., Reason, C. J., & Lutjeharms, J. R. (2009). Modes of the southern extension of the east Madagascar current. *Journal of Geophysical Research*, *114*(C1). https://doi.org/10.1029/2008JC004921

Siedler, G., Rouault, M., & Lutjeharms, J. R. (2006). Structure and origin of the subtropical south Indian Ocean countercurrent. *Geophysical Research Letters*, *33*(24). https://doi.org/10.1029/2006GL027399

Singh, A., Yadav, A., & Rana, A. (2013). K-means with three different distance metrics. *International Journal of Computer Applications*, *67*(10). https://doi.org/10.5120/11430-6785

Sprintall, J., Chong, J., Syamsudin, F., Morawitz, W., Hautala, S., Bray, N., & Wijffels, S. (1999). Dynamics of the south java current in the Indo-Australian basin. *Geophysical Research Letters*, *26*(16), 2493–2496. https://doi.org/10.1029/1999gl002320

Sprintall, J., Wijffels, S. E., Molcard, R., & Jaya, I. (2009). Direct estimates of the Indonesian Throughflow entering the Indian Ocean: 2004–2006. *Journal of Geophysical Research*, *114*(C7). https://doi.org/10.1029/2008jc005257

Srokosz, M., Robinson, J., McGrain, H., Popova, E., & Yool, A. (2015). Could the Madagascar bloom be fertilized by Madagascar iron? *Journal of Geophysical Research: Oceans*, *120*(8), 5790–5803. https://doi.org/10.1002/2015jc011075

Swallow, J. C., Fieux, M., & Schott, F. (1988). The boundary currents east and north of Madagascar: 1. geostrophic currents and transports. *Journal of Geophysical Research: Oceans*, *93*(C5), 4951–4962. https://doi.org/10.1029/jc093ic05p04951

Swallow, J. C., Schott, F., & Fieux, M. (1991). Structure and transport of the east African coastal current. *Journal of Geophysical Research: Oceans*, *96*(C12), 22245–22257. https://doi.org/10.1029/91jc01942

Talley, L. D. (2013). Closure of the global overturning circulation through the Indian, Pacific, and Southern Oceans: Schematics and transports. *Oceanography*, *26*(1), 80–97. https://doi.org/10.5670/oceanog.2013.07

Ternon, J.-F., Roberts, M., Morris, T., Hancke, L., & Backeberg, B. (2014). In situ measured current structures of the eddy field in the Mozambique channel. *Deep Sea Research Part II: Topical Studies in Oceanography*, *100*, 10–26. https://doi.org/10.1016/j.dsr2.2013.10.013

White, C., Selkoe, K. A., Watson, J., Siegel, D. A., Zacherl, D. C., & Toonen, R. J. (2010). Ocean currents help explain population genetic structure. *Proceedings of the Royal Society B: Biological Sciences*, *277*(1688), 1685–1694. https://doi.org/10.1098/rspb.2009.2214

Wyrtki, K. (1973). Physical oceanography of the Indian Ocean. In *The biology of the Indian Ocean* (pp. 18–36). Springer. https://doi.org/10.1007/978-3-642-65468-8_3

Ye, J., Zhao, Z., & Liu, H. (2007). Adaptive distance metric learning for clustering. In *2007 IEEE Conference on Computer Vision and Pattern Recognition* (pp. 1–7). https://doi.org/10.1109/cvpr.2007.383103